

Numerical aspects of Casimir energy computation in acoustic scattering

Xiaoshu Sun^{a,*}, Timo Betcke^a, Alexander Strohmaier^b

^a*Department of Mathematics, University College London, London, WC1E 6BT, UK*

^b*School of Mathematics, University of Leeds, Leeds, LS2 9JT, UK*

Abstract

Computing the Casimir force and energy between objects is a classical problem of quantum theory going back to the 1940s. Several different approaches have been developed in the literature often based on different physical principles. Most notably a representation of the Casimir energy in terms of determinants of boundary layer operators makes it accessible to a numerical approach. In this paper, we first give an overview of the various methods and discuss the connection to the Krein-spectral shift function and computational aspects. We present a new numerical scheme for the computation of the Casimir energy for large scale problems, which is based on the spectral properties of the block matrices for the boundary layer operators. This method allows for Casimir energy calculation for large-scale practical problems and significantly speeds up the computations in that case.

Keywords: Krein spectral shift function, Casimir energy, Krylov subspace, inverse-free generalized eigenvalue problem, Bempp-cl

1. Introduction

Casimir interactions are forces between objects such as perfect conductors. Hendrik Casimir predicted and computed this effect in the special case of two planar conductors in 1948 using a divergent formula for the zero point energy and applying regularisation to it [1]. This resulted in the famous formula for the attractive Casimir force per unit area

$$F(a) = -\frac{1}{A} \frac{\partial \mathcal{E}}{\partial a} = -\frac{\hbar c \pi^2}{240 a^4},$$

between two perfectly conducting plates, where A is the cross-sectional area of the boundary plates and \mathcal{E} is the Casimir energy as computed from a zeta regularised mode sum. The result here is for the electromagnetic field which differs by a factor of two from the force resulting from a massless scalar field. This force was measured experimentally by Sparnaay about 10 years later [2] and the Casimir effect has since become famous for its intriguing derivation and its counterintuitive nature. In 1996, precision measurements of the Casimir force between extended bodies were conducted by S.K. Lamoreaux [3] confirming the theoretical predictions including corrections for realistic materials. From 2000 to 2008, the Casimir force has been measured in various experimental configurations, such as cylinder-cylinder [4], plate-plate [5], sphere-plate [6] and sphere-comb [7]. The presence of the Casimir force has also been quoted as evidence for the zero point energy of the vacuum having direct physical significance. The classical way to compute Casimir forces mimicks Casimir's original computation and is based on zeta function regularisation of the vacuum energy. This has been carried out for a number of particular geometric situations (see [8, 9, 10, 11, 12] and references therein). The derivations are usually based on special functions and their properties and require explicit knowledge of the spectrum of the Laplace operator.

*Corresponding author

Email addresses: xiaoshu.sun.18@ucl.ac.uk (Xiaoshu Sun), t.betcke@ucl.ac.uk (Timo Betcke), a.strohmaier@leeds.ac.uk (Alexander Strohmaier)

In 1960s, Lifshitz and collaborators extended and modified this theory to the case of dielectric media [13] gave derivations based on the stress energy tensor. It has also been realised by quantum field theorists (see e.g. [14, 13, 15, 16, 17]) with various degrees of mathematical rigour that the stress energy approach yields Casimir's formula directly without the need for renormalisation or artificial regularisation. This tensor is defined by comparing the induced vacuum states of the quantum field with boundary conditions and the free theory. Once the renormalised stress energy tensor is mathematically defined, the computation of the Casimir energy density becomes a problem of spectral geometry (see e.g. [18]). The renormalised stress energy tensor and its relation to the Casimir effect can be understood at the level of rigour of axiomatic algebraic quantum field theory. We note however that the computation of the local energy density is non-local and requires some knowledge of the spectral resolution of the Laplace operator, the corresponding problem of numerical analysis is therefore extremely hard.

Lifshitz and collaborators also offered an alternative description based on the van der Waals forces between molecules. The plates consist of a collection of atomic-scale electric dipoles randomly oriented in the absence of the external forcing field. Quantum and thermal fluctuations may make the dipoles align spontaneously, resulting in a net electric dipole moment. The dipoles in the opposite plate feel this field across the gap and align as well. The two net electric dipole moments make the two plates attract each other. This approach emphasizes the influence from the materials more than the fluctuations in the empty space between the plates.

Somewhat independently from the spectral approach determinant formulae based on the van der Waal's mechanism were derived by various authors. We note here Renne [19] who gives a determinant formula for the van der Waals force based on microscopic considerations. Various other authors give path-integral considerations based on considerations of surface current fluctuations [20, 21, 22, 23, 24, 25, 26, 27, 28]. The final formulae proved suitable for numerical schemes and were also very useful to obtain asymptotic formulae for Casimir forces for large and small separations. The mathematical relation between the various approaches remained unclear, with proofs of equality only available in special cases. A full mathematical justification of the determinant formulae as the trace of an operator describing the Casimir energy was only recently achieved in [29] for the scalar field and [30] for the electromagnetic field. It was also proved recently in [31] that the formulae arising from Zeta regularisation, from the stress energy tensor, and from the determinant of the single layer operator all give the same Casimir forces.

We will now describe the precise mathematical setting and review the theory. Let $\Omega \subset \mathbb{R}^d$ be a non-empty bounded open subset with Lipschitz boundary $\partial\Omega$, which is the union of connected open sets Ω_j , for $j = 1, \dots, N$. We assume that the complement $\mathbb{R}^d \setminus \Omega$ of Ω is connected and the closures of Ω_j are pairwise non-intersecting. We denote the N connected components of the boundary $\partial\Omega$ by $\partial\Omega_j$. We will think of the open set Ω as a collection of objects Ω_j placed in \mathbb{R}^d and will refer to them as *obstacles*.

Then, several unbounded self-adjoint operators densely defined in $L^2(\mathbb{R}^d)$ can be defined.

- The operator Δ is the Laplace operator with Dirichlet boundary conditions on $\partial\Omega$.
- For $j = 1, \dots, N$, the operator Δ_j is the Laplace operator with Dirichlet boundary conditions on $\partial\Omega_j$.
- The operator Δ_0 is the “free” Laplace operator on \mathbb{R}^d with domain $H^2(\mathbb{R}^d)$.

These operators contain the dense set $C_0^\infty(\mathbb{R}^d \setminus \partial\Omega)$ in their domains. If $f : \mathbb{R} \rightarrow \mathbb{R}$ is a polynomially bounded function this set is also contained in the domain of the operators $f(\Delta^{\frac{1}{2}})$, $f(\Delta_j^{\frac{1}{2}})$, and $f(\Delta_0^{\frac{1}{2}})$, in particular the operator

$$D_f = f(\Delta^{\frac{1}{2}}) - f(\Delta_0^{\frac{1}{2}}) - \left(\sum_{j=1}^N [f(\Delta_j^{\frac{1}{2}}) - f(\Delta_0^{\frac{1}{2}})] \right)$$

is densely defined. It was shown in [29] that under additional analyticity assumptions on f the operator D_f is bounded and extends by continuity to a trace-class operator on $L^2(\mathbb{R}^d)$. These analyticity assumptions are in particular satisfied by $f(k) = (k^2 + m^2)^{\frac{s}{2}}$ for any $s > 0, m \geq 0$ and one has

$$\text{Tr}(D_f) = \frac{s}{\pi} \sin\left(\frac{\pi}{2}s\right) \int_m^\infty k(k^2 + m^2)^{\frac{s}{2}-1} \Xi(ik) dk, \quad (1)$$

where the function Ξ is given by

$$\Xi(k) = \log \det V_k \tilde{V}_k^{-1}$$

and the operators V_k and \tilde{V}_k are certain boundary layer operators that will be defined later. It was proved in [29] that the above determinant is well-defined in the sense of Fredholm as the operator $V_k \tilde{V}_k^{-1}$ near the positive imaginary axis differs from the identity operator by a trace-class operator on the Sobolev space $H^{\frac{1}{2}}(\partial\Omega)$. We remark here that the paper [29] assumed the boundary to be smooth and the operators $V_k \tilde{V}_k^{-1}$ was considered as a map on $L^2(\partial\Omega)$. The main result of the paper also holds for Lipschitz boundaries if $L^2(\partial\Omega)$ is replaced by $H^{\frac{1}{2}}(\partial\Omega)$. This requires minor modifications of the proof but we will not discuss this further here, as we are now focusing on computational aspects.

We also recall that by the Birman-Krein formula we have for any even function $h \in \mathcal{S}(\mathbb{R})$ the equality

$$\text{Tr}\left(h(\Delta^{\frac{1}{2}}) - h(\Delta_0^{\frac{1}{2}}) - \left(\sum_{j=1}^N [h(\Delta_j^{\frac{1}{2}}) - h(\Delta_0^{\frac{1}{2}})]\right)\right) = \int_0^\infty h'(k) \xi(k) dk, \quad (2)$$

where

$$\xi(k) = \frac{1}{2\pi i} \log\left(\frac{\det(S(k))}{\det(S_{1,k}) \cdots \det(S_{N,k}(k))}\right)$$

will be called the relative Krein spectral shift function. Here, $S_{j,k}$ are the scattering matrices of Δ_j associated to the objects Ω_j . Note here that the class of functions for which this is true can be relaxed to a certain extent, but even the most general version does not allow unbounded functions such as $f(k)$ with $s > 0, m \geq 0$. The relative spectral shift function can however be related via a Laplace transform to the Fourier transform of the relative spectral shift function (see [32]). Under mild convexity assumptions this can be connected to the Duistermaat-Guillemain trace formula in obstacle scattering theory to give an asymptotic expansion of $\Xi(k)$ in terms of the minimal distance $\delta > 0$ between the obstacles and the linearised Poincaré map of the bouncing ball orbits between the obstacles of that length. One has

$$\Xi(k) = - \sum_j \frac{1}{|\det(I - P_{\gamma_j})|^{\frac{1}{2}}} e^{2i\delta k} + o(e^{-2\delta \text{Im} k}),$$

where the sum is over bouncing ball modes of length 2δ and P_{γ_j} is the associated Poincaré map, where γ_j is the shortest bouncing ball orbits.

The Casimir energy of the configuration Ω for a massless scalar field would then be given by D_f in the case when $f(k) = k$ and is therefore equal to

$$\zeta = \frac{\hbar c}{2\pi} \int_0^\infty \Xi(ik) dk.$$

In this paper, we are going to introduce the numerical framework of computing the Casimir energy based on the evaluation of the log determinant of the integral operators in the acoustic case ¹ in Section 2. Afterwards, two efficient methods for computing the integrand of the Casimir energy will be illustrated in Section 3 which makes us compute the large-scale problem efficiently. In Section 4, several examples on computing the Casimir

¹The mathematical theories and numerical experiments in the Maxwell case have been done as well and they will be reported in another paper.

energy between the compact objects will be shown and we will also compare our results with others computed in other methods. Note that all the tests and examples in this paper were computed with version 0.2.4 of the Bempp-cl library [33]. Finally, Section 5 will conclude our paper and discuss the future plan as well.

2. Numerical methods for computing the Casimir energy in acoustic scattering

In this section, we give details of computing the Casimir energy via boundary integral operator discretisations. Assume $\Omega^- \subset \mathbb{R}^d$, for $d \geq 2$ is the interior bounded Lebesgue-measurable domain that the scatterer occupies with piecewise smooth Lipschitz boundary Γ . The exterior domain is denoted as $\Omega^+ = \mathbb{R}^d \setminus \overline{\Omega^-}$. \mathbf{n} is the exterior unit normal to the surface Γ pointing outwards from Ω^- and \mathbf{n}_x is normal to Γ at the point $x \in \Gamma$.

In the scalar case, the Casimir energy can be expressed in terms of certain single-layer boundary operator, which we will define below. We then present its relationship with the Krein-Spectral shift function and demonstrate how it can practically be computed.

2.1. The single-layer boundary operator

For the bounded interior domain Ω^- or the unbounded exterior domain Ω^+ , the space of the (locally) square integrable functions is

$$L^2(\Omega^-) := \left\{ f : \Omega^- \rightarrow \mathbb{C}, f \text{ is Lebesgue measurable and } \int_{\Omega^-} |f|^2 < \infty \right\},$$

$$L^2_{\text{loc}}(\Omega^+) := \left\{ f : \Omega^+ \rightarrow \mathbb{C}, f \text{ is Lebesgue measurable and } \int_K |f|^2 < \infty, \text{ for all compact } K \subset \Omega^+ \right\}$$

and note that the subscript ‘‘loc’’ can be removed if the domain is bounded (i.e. $L^2_{\text{loc}}(\Omega^-) = L^2(\Omega^-)$). We define the (local) Sobolev space $H_{\text{loc}}^s(\Omega^\pm)$ as

$$H_{\text{loc}}^s(\Omega^\pm) := \left\{ f \in L^2_{\text{loc}}(\Omega^\pm), \forall \alpha \text{ s.t. } |\alpha| \leq s, D^\alpha f \in L^2_{\text{loc}}(\Omega^\pm) \right\},$$

where $\alpha = (\alpha_1, \alpha_2, \dots, \alpha_d)$ is a multi-index and $|\alpha| = \alpha_1 + \alpha_2 + \dots + \alpha_d$, and the derivative is defined in the weak sense.

For any function $f \in H_{\text{loc}}^1(\Omega)$ we can define the trace γ_D^\pm as

$$\gamma_D^\pm p(\mathbf{x}) := \lim_{\Omega^\pm \ni \mathbf{x}' \rightarrow \mathbf{x} \in \Gamma} p(\mathbf{x}').$$

We call the range of the trace operator $H^{1/2}(\Gamma)$. This space can be more rigorously defined. But for the purposes of this paper the description of $H^{1/2}(\Gamma)$ is range space of the trace operator is sufficient. We furthermore need the space $H^{-1/2}(\Gamma)$, which is the dual space of $H^{1/2}(\Gamma)$ with $L^2(\Gamma)$ as pivot space.

We can now define the single-layer boundary $V_k : H^{-1/2}(\Gamma) \rightarrow H^{1/2}(\Gamma)$ as

$$(V_k \mu)(\mathbf{x}) := \int_{\Gamma} g_k(\mathbf{x}, \mathbf{y}) \psi(\mathbf{y}) dS_{\mathbf{y}}, \quad \text{for } \mu \in H^{-1/2}(\Gamma) \text{ and } \mathbf{x} \in \Gamma.$$

Here,

$$g_k(\mathbf{x}, \mathbf{y}) = \begin{cases} \frac{i}{4} H_0^{(1)}(k|\mathbf{x} - \mathbf{y}|), & \text{for } d = 2 \\ \frac{e^{ik|\mathbf{x} - \mathbf{y}|}}{4\pi|\mathbf{x} - \mathbf{y}|}, & \text{for } d = 3, \end{cases} \quad (3)$$

with $H_0^{(1)}$ a Hankel function of the first kind.

2.2. The formula of the Casimir energy

Before we present the formula of the Casimir energy, let us introduce the following theorem.

Theorem 1. [29] Consider Ω as a domain assembling from individual objects Ω_i . Let V_k be the single-layer boundary operator defined on the boundary $\partial\Omega = \bigcup_{i=1}^N \partial\Omega_i$, and \tilde{V}_k is the “diagonal part” of V_k by restricting the integral kernel to the subset $\bigcup_{i=1}^N \partial\Omega_i \times \partial\Omega_i \subset \partial\Omega \times \partial\Omega$ then the operator $V_k \tilde{V}_k^{-1} - I$ with I the identity operator is trace-class and

$$\Xi(k) = \log \det(V_k \tilde{V}_k^{-1}),$$

where the Fredholm determinant $\det(V_k \tilde{V}_k^{-1})$ is well-defined². and by taking $m = 0$ and $s = 1$ in (1), this gives the formula

$$\text{Tr} \left(\Delta^{\frac{1}{2}} + (N-1)\Delta_0^{\frac{1}{2}} - \sum_{i=1}^N \Delta_j^{\frac{1}{2}} \right) = \frac{1}{\pi} \int_0^\infty \Xi(ik) dk. \quad (4)$$

Equation (4) is used to compute the Casimir energy between the objects and the formula is written as

$$\zeta = \frac{\hbar c}{2\pi} \int_0^\infty \Xi(ik) dk. \quad (5)$$

This formula is the same with the one proposed in the numerical work by Johnson et al. who derive this formula by ill-defined path integrals[35], which makes it non-rigorous.

Remark 1. There is a relation between the relative Krein spectral shift function and the single-layer boundary integral operator. That is, for $k > 0$,

$$-\frac{1}{\pi} \text{Im}\Xi(k) = \frac{i}{2\pi} (\Xi(k) - \Xi(-k)) = \xi(k).$$

2.3. Galerkin discretization and boundary element spaces

In order to compute the integral (5), we need to compute the log determinant of the operators $V_k \tilde{V}_k^{-1}$. In this section we discuss Galerkin discretisations to compute this quantity.

Define the triangulation \mathcal{T}_h of the boundary surface Γ with triangular surface elements τ_l and associated nodes \mathbf{x}_i s.t. $\overline{\mathcal{T}_h} = \bigcup_l \overline{\tau_l}$, where h is the mesh size and define the space of the continuous piecewise linear functions

$$P_h^1(\Gamma) = \{v_h \in C^0(\Gamma) : v_h|_{\tau_l} \in \mathbb{P}_1(\tau_l), \text{ for } \tau_l \in \mathcal{T}_h\},$$

where $\mathbb{P}_1(\tau_l)$ denotes the space of polynomials of order less than or equal to 1 on τ_ℓ . We have

$$P_h^1(\Gamma) := \text{span}\{\phi_j\} \subset H^{-\frac{1}{2}}(\Gamma)$$

with

$$\phi_j(\mathbf{x}_i) = \begin{cases} 1, & i = j, \\ 0, & i \neq j \end{cases}$$

being the nodal basis functions.

²The Fredholm determinant is a generalization of a determinant of finite dimensional matrix to finite dimensional linear operator which differ from the identity operator by a trace class operator [34, Section 6.5.2]. Since the operator $V_k \tilde{V}_k^{-1} - I$ with I the identity operator is trace-class in the close upper half space [29, Theorem 1.7], the determinant $\det(V_k \tilde{V}_k^{-1})$ is well-defined.

Remark 2. Since $H^{-1/2}(\Gamma)$ does not require continuity we could use a space of simple piecewise constant functions. The reason why we choose piecewise linear functions is the size of the arising matrix systems for dense calculations. The computation of the log-determinant requires $\mathcal{O}(n^3)$ operations, where n is the dimension of our approximation basis. For sphere-like and other similar geometries there are in practice roughly twice as many triangles as nodes in the mesh. Hence, while the assembly cost with piecewise linear functions is higher, the resulting matrix has only half the dimension, resulting in roughly a factor eight reduction of computational complexity for the log determinant. A disadvantage is that on geometries with corners or edges the converges close to these singularities is suboptimal with continuous piecewise linear functions.

Having defined the basis function ϕ_j , we can represent each element inside the Galerkin discretization form. Assume there are N objects, then the matrix of the operator V_k is an N by N block matrix, written as

$$V(k) = \begin{bmatrix} V_{11}(k) & V_{12}(k) & \cdots & V_{1N}(k) \\ V_{21}(k) & V_{22}(k) & \cdots & V_{2N}(k) \\ \vdots & \vdots & \ddots & \vdots \\ V_{N1}(k) & V_{N2}(k) & \cdots & V_{NN}(k) \end{bmatrix} \quad (6)$$

and the matrix \tilde{V}_k is the diagonal part of V_k :

$$\tilde{V}(k) = \begin{bmatrix} V_{11}(k) & 0 & \cdots & 0 \\ 0 & V_{22}(k) & \cdots & 0 \\ \vdots & \vdots & \ddots & \vdots \\ 0 & 0 & \cdots & V_{NN}(k) \end{bmatrix}. \quad (7)$$

Therefore, the element in the m th row and n th column of the block matrix $V_{ij}(k)$ is

$$V_{ij}^{(m,n)}(k) = \langle V_{ij}(k)\phi_n^{(j)}, \phi_m^{(i)} \rangle = \int_{\Gamma_j} \overline{\phi_m^{(i)}}(\mathbf{x}) \int_{\Gamma_i} g_k(\mathbf{x}, \mathbf{y}) \phi_n^{(j)}(\mathbf{y}) dS_{\mathbf{y}} dS_{\mathbf{x}}, \quad (8)$$

where $\boldsymbol{\phi}^{(i)} = [\phi_1^{(i)} \quad \phi_2^{(i)} \quad \dots \quad \phi_N^{(i)}]$ is the set of basis functions defined on the i th object and

$$\langle f, g \rangle = \int_{\Gamma} f(\mathbf{x}) \overline{g(\mathbf{x})} dS_{\mathbf{x}}$$

denotes the standard $L^2(\Gamma)$ inner product.

The value of $\Xi(ik) = \log \det(V(ik)\tilde{V}(ik)^{-1})$ can now be explicitly computed by evaluating the corresponding log determinants.

The function $\Xi(ik)$ has a very favourable decay behaviour for growing k that we can use to limit the number of quadrature points necessary to evaluate the corresponding Casimir integral, namely under certain convexity assumptions on the obstacles it holds that

$$\Xi(ik) = \mathcal{O}(e^{-2Zk}).$$

Here, Z is the minimum distance between the obstacles [36, Theorem 4.1].

This result can be justified heuristically, using a simple matrix perturbation argument. Consider a symmetric matrix A partitioned as

$$A = \begin{bmatrix} A_1 & 0 \\ 0 & A_2 \end{bmatrix}.$$

and a symmetric matrix E partitioned as

$$E = \begin{bmatrix} 0 & E_1^T \\ E_1 & 0 \end{bmatrix}$$

Then it holds for the i th eigenvalue $\lambda_i(A)$ and the i th eigenvalue $\lambda_i(A + E)$ that

$$|\lambda_i(A) - \lambda_i(A + E)| \leq \frac{\|E\|^2}{\text{gap}_i},$$

where gap_i is the distance of $\lambda_i(A)$ to the spectrum of A_2 if $\lambda_i(A)$ is an eigenvalue of A_1 , and to the spectrum of A_1 if $\lambda_i(A)$ is an eigenvalue of A_2 . Details can be found in [37].

Now assume that we have two different obstacles. Then we have $A_1 = V_{11}(k)$, $A_2 = V_{22}(k)$ and $E_1 = V_{21}$ as the matrix of cross interactions between the two obstacles. The Green's function between two obstacles decays exponentially like e^{-Zk} , where Z is the minimal distance between them, resulting in a matrix perturbation result of the form $|\lambda_i(V) - \lambda_i(\tilde{V})| = O(e^{-2Zk})$ for increasing k (see Figure), from which the corresponding perturbation result for the log determinant follows.

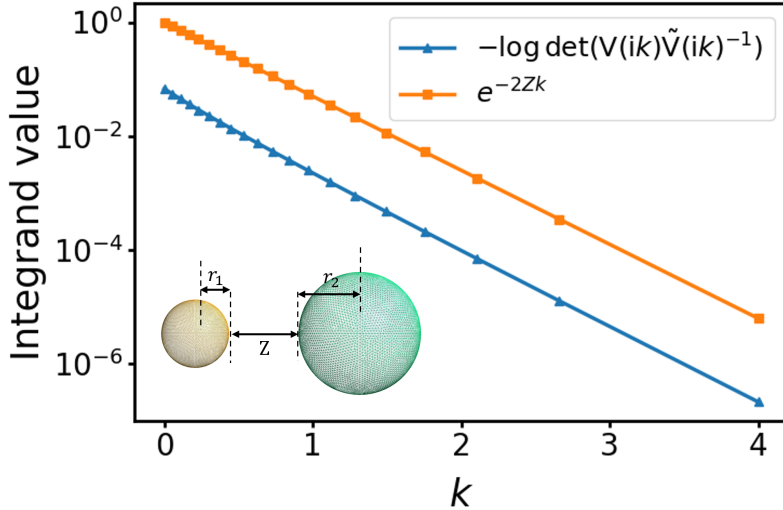


Figure 1: Exponential decay of $\Xi(ik)$ for two distinct spheres with radii $r_1 = 0.5$ and $r_2 = 1$ and minimum distance $Z = 1.5$. The red line is the decay bound and the blue line is the actual decay.

This purely linear algebraic consideration is not fully robust as it ignores the importance of the eigenvalue gap in the perturbation result. But we can heuristically explain the gap as follows. On the continuous level the perturbations E_1 and E_2 are compact, so the tail end of the spectrum that converges to zero with small values of gap_i , is little affected by E , and the corresponding eigenvalues have a contribution of $\log \left| \frac{\lambda_i(A)}{\lambda_i(A+E)} \right| \approx 0$ to the value of Ξ . The relevant eigenvalues are the larger ones who for distinct obstacles have a sufficiently large value of gap_i .

While the linear algebra argument is useful to give a heuristical explanation, it is not as rigorous as the analytical result in [36]. In particular, we want to emphasize that the exponential decay bound with the quadratic factor also holds if the two obstacles are identical, which is not obvious from pure linear algebraic considerations. An example of this is given in Figure 2.

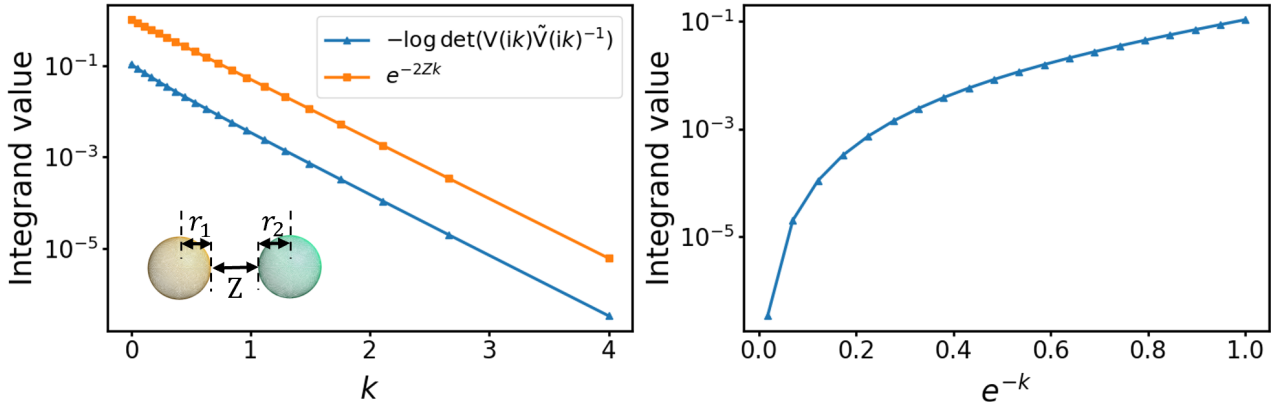


Figure 2: (Left) Exponential decay of $\Xi(ik)$ for two identical spheres with radius $r_1 = r_2 = 1$ and minimum distance $Z = 1.5$. The red line is the decay bound and the blue line is the actual decay. (Right) The integrand $\Xi(ik)$ after variable transformation to apply a numerical trapezoid rule for its evaluation.

This nice numerical property for the integrand $\Xi(ik)$ simplifies the numerical integration. One can apply the normal trapezoidal rule to calculate the integral $\int_0^\infty \Xi(ik) dk = \int_0^\infty \log \frac{\det V(ik)}{\det \tilde{V}(ik)} dk$ with k changed to y with $y = e^{-k}$. Figure 2 (Right) plots the integrand with regard to the new variable y .

3. Efficient methods for computing $\log \det(V(ik)\tilde{V}(ik)^{-1})$

By Section 2, to compute the Casimir energy, it is necessary to evaluate the term $\log \det(V(ik)\tilde{V}(ik)^{-1})$ with different values of k . In this section, several efficient methods will be introduced to compute this log determinant.

The log determinant of the matrix $V(ik)\tilde{V}(ik)^{-1}$ is equal to the sum of the logarithm of the eigenvalues of $V(ik)\tilde{V}(ik)^{-1}$. Since $\tilde{V}(ik)$ is a compact perturbation of $V(ik)$, most of the eigenvalues of the matrix $V(ik)\tilde{V}(ik)^{-1}$ are close to 1 (shown in Figure 3) and contribute little to the value of the Casimir energy. Hence, we do not need to compute all eigenvalues but only the extremal ones, making subspace methods such as Krylov solvers attractive for this problem.

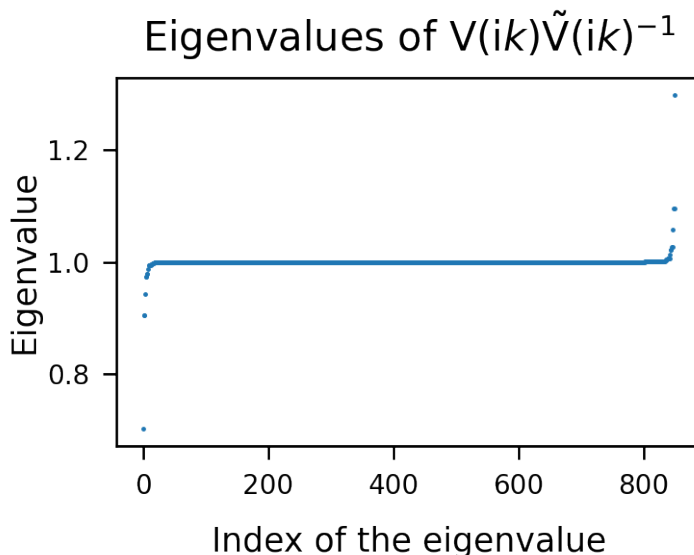


Figure 3: The eigenvalues of the matrix $V(ik)\tilde{V}(ik)^{-1}$ when $ik = 0.8i$. The scatterers are two spheres with equal radii $r_1 = r_2 = 1$ and the minimal distance between them is $Z = 0.5$. The grid size of the mesh is $h = 0.2$.

In what follows we demonstrate and compare iterative solver approaches based on standard Arnoldi iterations

[38, 39], and based on the inverse free Krylov subspace method [40, 41]. We will also discuss on acceleration strategy which is based on the idea of recycling projection bases from one quadrature point to the next.

3.1. Method I: Standard Arnoldi method

The first efficient method for solving our eigenvalue problem $\mathbf{V}(ik)\tilde{\mathbf{V}}(ik)^{-1}\mathbf{x} = \lambda\mathbf{x}$ is the Arnoldi method [39, Section 6.2]. The idea of this method is to use Arnoldi iterations to construct the Krylov subspace $K_m(\mathbf{V}(ik)\tilde{\mathbf{V}}(ik)^{-1}, \mathbf{b})$, where \mathbf{b} is some initial vector and m is the dimension of this Krylov subspace, and to then compute the eigenvalues of the resulting projected Hessenberg matrix H_m (see [42]). These eigenvalues have a good approximation on the extreme eigenvalues of $\mathbf{V}(ik)\tilde{\mathbf{V}}(ik)^{-1}$ [39, Proposition 6.10, Theorem 6.8].

The main cost of this standard Arnoldi method is the computation of the Krylov subspace K_m . In this process, one has to compute the matrix-vector product $\tilde{\mathbf{V}}^{-1}\mathbf{y}$, for some vector \mathbf{y} , which is equivalent to solve the linear system $\tilde{\mathbf{V}}\mathbf{x} = \mathbf{y}$. This can be efficiently implemented as the matrix $\tilde{\mathbf{V}}$ is a block diagonal matrix. Therefore, we just need to compute the LU decomposition for each diagonal block, \mathbf{V}_{jj} rather than the whole system matrix and apply the forward and backward substitution to solve the linear system $\mathbf{V}_{jj}\mathbf{x}_j = \mathbf{y}_j$. Note that if all the scatterers are identical, one only needs to compute one diagonal block and one LU decomposition.

3.2. Method II: Inverse-free Krylov subspace method

An alternative to the standard Arnoldi method is the inverse-free projection method, which is also based on the Arnoldi iterations but without computing any matrix inversions. Consider the eigenvalue problem $\mathbf{V}(ik)\tilde{\mathbf{V}}(ik)^{-1}\mathbf{x} = \lambda\mathbf{x}$, it is equivalent to the following generalized eigenvalue problem:

$$\mathbf{V}(ik)\tilde{\mathbf{x}} = \lambda\tilde{\mathbf{V}}(ik)\tilde{\mathbf{x}}. \quad (9)$$

An important property of this problem is that as we are only interested in ik along the imaginary axis, the corresponding matrix $\tilde{\mathbf{V}}(ik)$ is positive definite, and $\mathbf{V}(ik)$ is still symmetric.

In [40, 41], the authors proposed an inverse-free Krylov subspace method for computing a few extreme eigenvalues of the symmetric definite generalized eigenvalue problem. The following algorithm summarizes the method.

Algorithm 1: Inverse-free Krylov subspace method for computing multiple extreme eigenvalues of the generalized eigenvalue problem $A\mathbf{x} = \lambda B\mathbf{x}$

Input: Symmetric matrix $A \in \mathbb{R}^{n \times n}$, s.p.d matrix $B \in \mathbb{R}^{n \times n}$, an initial approximation \mathbf{x} with $\|\mathbf{x}\| = 1$,

a given shift ρ and the dimension of the Krylov subspace $m \geq 1$

Output: A set of approximate eigenvalues of $A\mathbf{x} = \lambda B\mathbf{x}$ and associated eigenvectors.

- 1: Construct a basis Z_m for the Krylov subspace $K_m = \text{span}(\mathbf{x}, (A - \rho B)\mathbf{x}, \dots, (A - \rho B)^{m-1}\mathbf{x})$ with dimension m
 - 2: Project A and B on Z : $A_m = Z_m^T(A - \rho B)Z_m$, $B_m = Z_m^TBZ_m$
 - 3: Compute all the eigenpairs $\{(\tilde{\lambda}_i, \mathbf{x}_i)\}_{i=1,\dots,m}$ for the matrix pencil (A_m, B_m)
 - 4: Reverse the shift to obtain $\lambda_i = \tilde{\lambda}_i + \rho$.
-

Algorithm 1 approximates m eigenvalues close to the shift ρ for the matrix pencil (A, B) , where m is the dimension of the Krylov subspace K_m in Step 1, Algorithm 1. The question is what shift strategy to use for ρ . In numerical experiments it turned out that for the KSSF problem choosing $\rho = 1$ sufficiently approximate the eigenvalues that have the main contribution to $\log \det(\mathbf{V}(ik_j)\tilde{\mathbf{V}}(ik_j)^{-1})$. Additionally, the main cost of this inverse free Krylov subspace method is the computation of the Krylov subspace and the projection of the matrices A and B . In our case these are large dense matrices representing integral operators.

3.3. Recycling Krylov subspace based variant

The main cost of the standard Arnoldi method and inverse-free method comes from the matrix-vector products (matvecs) in the Arnoldi iterations, where the involving matrices are large and dense as they represent discretized integral operators. In order to reduce the computational cost of a Krylov subspace basis for each wavenumber ik , we introduce a subspace recycling based method for speeding up the computational process. This can be regarded as a variant of these two methods.

This recycling strategy is based on the idea that a Krylov subspace for a previous quadrature point in the KSSF integral will be a good approximation to a Krylov subspace for the current quadrature point. We initially compute a Krylov basis for the wavenumber ik_1 associated with the first quadrature point. We then extract several eigenvectors associated with the extremal eigenvalues based on Algorithm 1 and then orthogonalize to obtain an initial approximation basis for the wavenumber ik_2 . For this wavenumber we project the matrices onto the recycled basis, compute approximate eigenpairs $(\tilde{\lambda}_i, \tilde{\mathbf{x}}_i)$ and then extend the subspace basis with the residuals $\mathbf{r}_i = \mathbf{V}(ik)\tilde{\mathbf{x}}_i - \tilde{\lambda}_i\tilde{\mathbf{V}}(ik)\tilde{\mathbf{x}}_i$. With the extended subspace we recompute the eigenpairs for the second wavenumber's case and extract eigenvectors as starting basis for the third wavenumber, and so on.

3.4. Numerical results

In this section, we compare the performance of standard Arnoldi and inverse-free Krylov subspace method and their recycled variants on computing the log determinant term of $\mathbf{V}(ik)\tilde{\mathbf{V}}(ik)^{-1}$. As the dominant cost of these methods is the matrix-vector products (matvec) associated with the discretized boundary integral operators, we will also compare the number of the matvecs between these methods. All the tests are performed on two spheres with equal radii $r_1 = r_2 = 1$. The sphere meshes are refined with size $h = 0.1$ and this results in the matrix size $\mathbf{V}(ik)$ being 3192×3192 . Again, the minimum distance between them is denoted by Z , which is set as 0.5, 1.5 and 3.0. The number of the quadrature points is 20.

We start by comparing the relative error for approximating the $\log \det \mathbf{V}(ik)\tilde{\mathbf{V}}(ik)^{-1}$ using all these methods. The dimension of the Krylov subspace K_m in all the algorithms is $m = 100$. For the methods with subspace recycled, the number of the recycled eigenvectors is not fixed but depends on the number of the relevant eigenvalues in each wavenumber case. In our experiments, we only recycle the eigenvector whose corresponding eigenvalue has the logarithm value greater than 10^{-s} , where $s = 3, 4, 5$ when $Z = 0.5, 1.5, 3.0$, respectively, in which case the estimates of the log determinant have at least three significant digits match with the ones obtained from the direct computations. With these settings, the number of the recycled eigenvectors becomes less and less as the k gets larger. Figure 4 plots the dimension of the extended subspace for each wavenumber case. It is equal to the number of the recycled eigenvectors plus the number of the residuals $\{\mathbf{r}_i\}_i$.

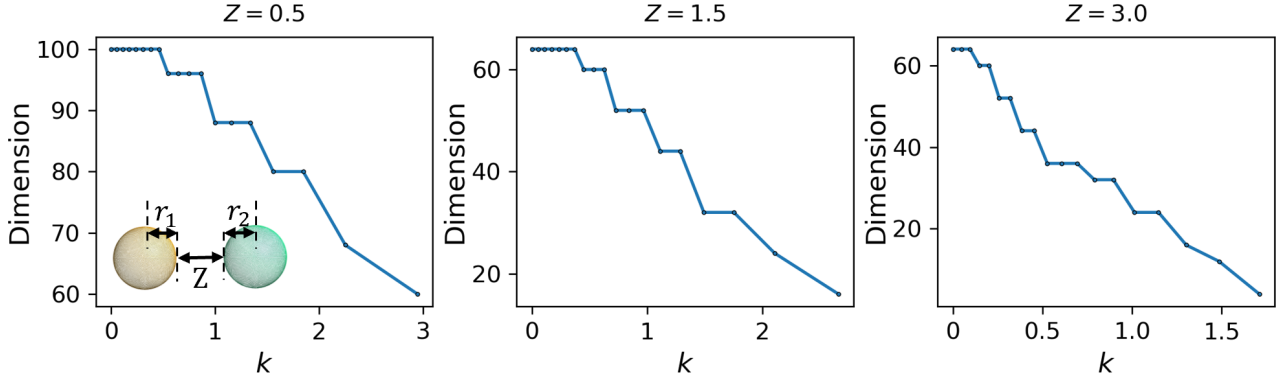


Figure 4: The dimension of the extended subspace in the inverse-free Krylov subspace/standard Arnoldi methods with subspace recycled for each k in $\log \det(V(ik)\tilde{V}(ik)^{-1})$, which is equal to the number of the recycled eigenvectors plus the number of the residuals $\{\mathbf{r}_i\}_i$. The recycled eigenvector has the corresponding eigenvalue whose logarithm is larger than 10^{-s} , where $s = 3, 4, 5$ when $Z = 0.5, 1.5, 3.0$, respectively.

Table 1 lists the relative error for approximating the value of $\log \det(V(ik)\tilde{V}(ik)^{-1})$ computed via the inverse-free Krylov subspace method and standard Arnoldi method with or without recycling the subspace. The reference value is computed by the direct dense computation of the log determinant. The wavenumbers ik are chosen to be associated with the first five consecutive quadrature points, whose corresponding log determinant values account for a great proportion in the Casimir integral.

This table indicates that with the settings above, one can have at least three significant digits accuracy and the performance of the methods with subspace recycled is similar to the ones without any recycling processes. As for the performance of these methods and their variants at larger quadrature points, we cannot always have three digits accuracy. However, this will not affect the estimates of the Casimir energy too much as their corresponding log determinant value is relatively smaller than the others and contributes very little to the Casimir energy.

Distance Z	Wavenumber k	Inverse-free (no recycling)	Inverse-free (recycling)	Standard Arnoldi (no recycling)	Standard Arnoldi (recycling)
$Z = 0.5$	0	9.79×10^{-4}	9.79×10^{-4}	9.29×10^{-4}	9.29×10^{-4}
	0.0540	9.67×10^{-4}	9.78×10^{-5}	4.91×10^{-5}	1.37×10^{-6}
	0.111	1.22×10^{-3}	2.79×10^{-5}	5.29×10^{-5}	5.17×10^{-6}
	0.171	1.15×10^{-3}	2.42×10^{-5}	2.78×10^{-5}	8.45×10^{-5}
	0.236	1.25×10^{-3}	9.10×10^{-6}	1.12×10^{-4}	2.76×10^{-5}
$Z = 1.5$	0	9.48×10^{-4}	9.54×10^{-4}	3.41×10^{-7}	3.41×10^{-7}
	0.0530	1.02×10^{-3}	2.87×10^{-4}	5.89×10^{-7}	3.97×10^{-8}
	0.109	1.16×10^{-3}	1.80×10^{-4}	1.45×10^{-8}	2.35×10^{-4}
	0.168	1.25×10^{-3}	1.35×10^{-4}	2.70×10^{-6}	1.06×10^{-4}
	0.231	1.33×10^{-3}	4.77×10^{-5}	3.14×10^{-7}	4.87×10^{-5}
$Z = 3.0$	0	1.38×10^{-3}	1.38×10^{-3}	8.55×10^{-12}	8.55×10^{-12}
	0.0465	1.54×10^{-3}	4.34×10^{-4}	3.46×10^{-9}	2.61×10^{-5}
	0.0954	1.81×10^{-3}	2.89×10^{-4}	5.02×10^{-10}	5.43×10^{-7}
	0.146	2.13×10^{-3}	2.35×10^{-4}	4.82×10^{-8}	2.50×10^{-5}
	0.200	2.54×10^{-3}	2.13×10^{-4}	5.07×10^{-9}	1.59×10^{-5}

Table 1: Relative error for approximating the value of $\log \det(V(ik)\tilde{V}(ik)^{-1})$ on the wavenumbers associated with the first five consecutive quadrature points via the inverse-free Krylov subspace and standard Arnoldi methods with/without subspace recycled. The shift is set as $\rho = 1$ for the inverse-free method. The recycled eigenvector has the corresponding eigenvalue whose logarithm is larger than 10^{-s} , where $s = 3, 4, 5$ when $Z = 0.5, 1.5, 3.0$, respectively.

Recall that the main cost in these algorithms is from the computation of the Krylov basis and the matrix projections. For large problems, the dominating cost is the involved matrix-vector products with the discretized integral operators. We count the number of matvecs associated with the discretized integral operators (V_{ij}) for each algorithm and the results are summarized in Table 2.

Inverse-free Krylov subspace method		Standard Arnoldi method	
Without recycling	With recycling	Without recycling	With recycling
$(6m - 2)N_q$	$(6m - 2) + 12 \sum_{i=1}^{N_q-1} s_i$	$(4m - 4)N_q$	$(4m - 4) + 8 \sum_{i=1}^{N_q-1} s_i$

Table 2: The number of matvecs associated with the discretized integral operators inside the inverse-free Krylov subspace and standard Arnoldi methods with or without recycling subspace. N_q is the number of wavenumbers/quadrature points, m is the dimension of the Krylov subspace for the first wavenumber (in recycling case); for all the wavenumbers (in non-recycling case), and s_i is the number of the recycled eigenvectors from the i th wavenumber's case (in recycling case)

In Figure 5, we plot the number of actual matvecs associated with the discretized matrix form V_{ij} , for $i, j = 1, 2, \dots, N$ in each individual algorithm when computing the Casimir energy between 2 spheres with different different distance Z . It shows that the recycling strategy significantly reduces the overall number of matvecs. Although the number of matvecs in standard Arnoldi method with subspace recycled (light red in Figure 5) is smaller than the one of the inverse-free method with subspace recycled (light blue in Figure 5), one has to compute the LU decomposition for each diagonal block in each Arnoldi iteration, which has cubic complexity.

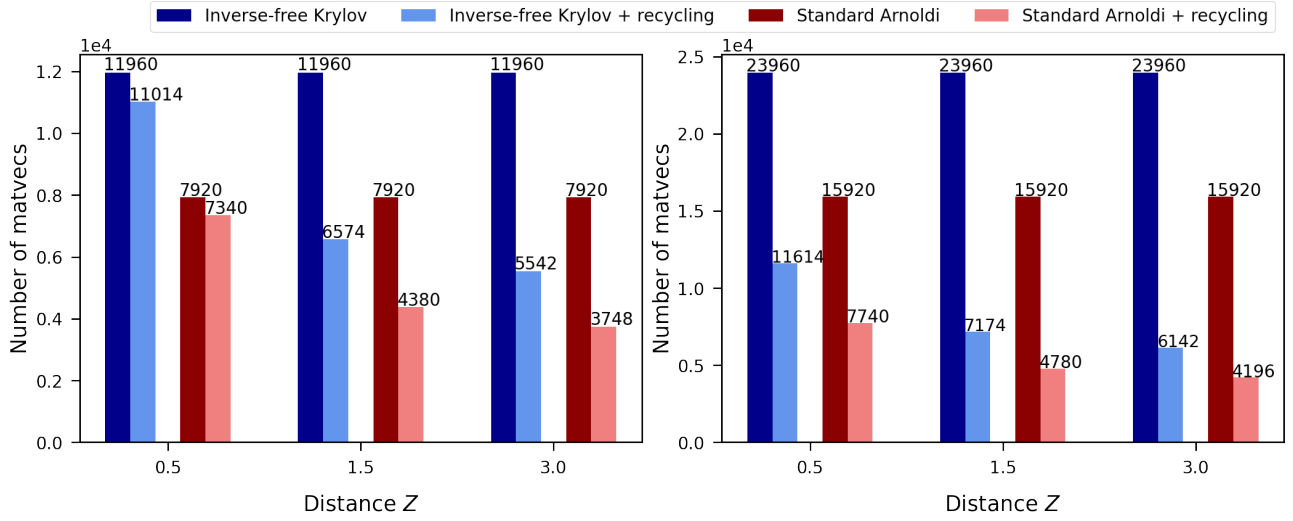


Figure 5: The number of matvecs inside the inverse-free and standard Arnoldi methods with or without recycling subspace when computing the normalized Casimir energy between two spheres with equal radii $R = 1$ and the distance Z is 0.5, 1.5 and 3.0. The number of the quadrature point is $N_q = 20$. The dimension of the Krylov subspace is set as $m = 100$ (Left) and 200 (Right).

4. Numerical experiments

In this section, we demonstrate numerical results for computing the Casimir energy between two conducting objects, where the objects are spheres, sphere-torus, Menger sponges, ice crystals and ellipsoids. One reference value of the Casimir energy is computed by the Richardson extrapolation method which is often used for obtaining the higher-order estimate at zero grid spacing.

In the case of spheres we also compare with known asymptotic expansions [24].

4.1. Sphere-sphere and sphere-torus case

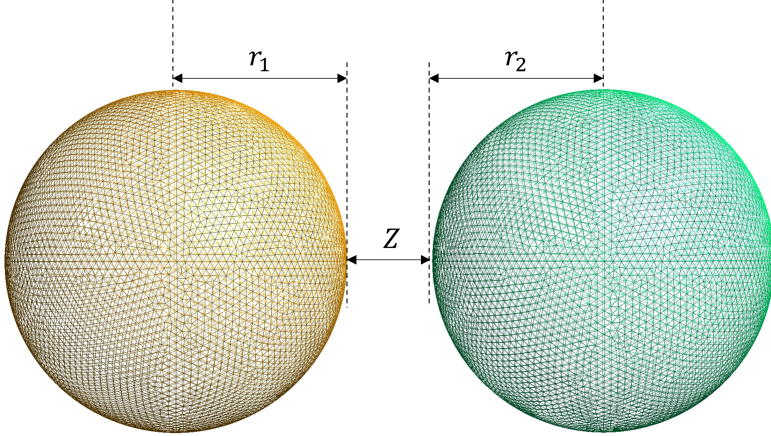


Figure 6: Two spheres with equal radii $r_1 = r_2 = 1$ and Z is the minimal distance between them.

$h_{\text{coarse}} = 0.1$: $\dim(V(ik)) = 3192$, N° of elements on both grids = 6384;

$h_{\text{fine}} = 0.05$: $\dim(V(ik)) = 12603$, N° of elements on both grids = 25180

Consider two spheres with the equal radii $r_1 = r_2 = 1$ and the spacing Z (see Figure 6) as the scatterers. We denote Ξ_h , the value of Ξ computed under the refinement level with mesh size h and denote $\Xi_{h=0}$, the higher-order estimate of Ξ_h at zero grid space, which is computed by Richardson extrapolation,

$$\Xi_{h=0} \approx \frac{h_{\text{coarse}}^2 \Xi_{h_{\text{fine}}} - h_{\text{fine}}^2 \Xi_{h_{\text{coarse}}}}{h_{\text{coarse}}^2 - h_{\text{fine}}^2}, \quad (10)$$

where h_{fine} and h_{coarse} are two different mesh sizes with $h_{\text{fine}} < h_{\text{coarse}}$. In this example, we set $h_{\text{coarse}} = 0.1$ and $h_{\text{fine}} = 0.05$.

We begin with validating the construction of the integrand function Ξ of the Casimir integral (5) by comparing the value of $\Xi_h(ik)$ for different refinement levels with the extrapolation value $\Xi_{h=0}$ for $ik = 0.8i$ (see Figure 7). In the tables of Figure 7, we also provide reference values computed by discretizing the single-layer boundary integral operators in terms of the spherical harmonic functions as suggested by [26]. They are believed to be accurate within 0.05%.

In Figure 7, one can see that $\Xi_h(ik)$ converges to $\Xi_{h=0}$ as h increases. This figure is plotted in log-log scale plot and the slope of these lines is around 2. This numerical result indicates that this convergence is quadratic.

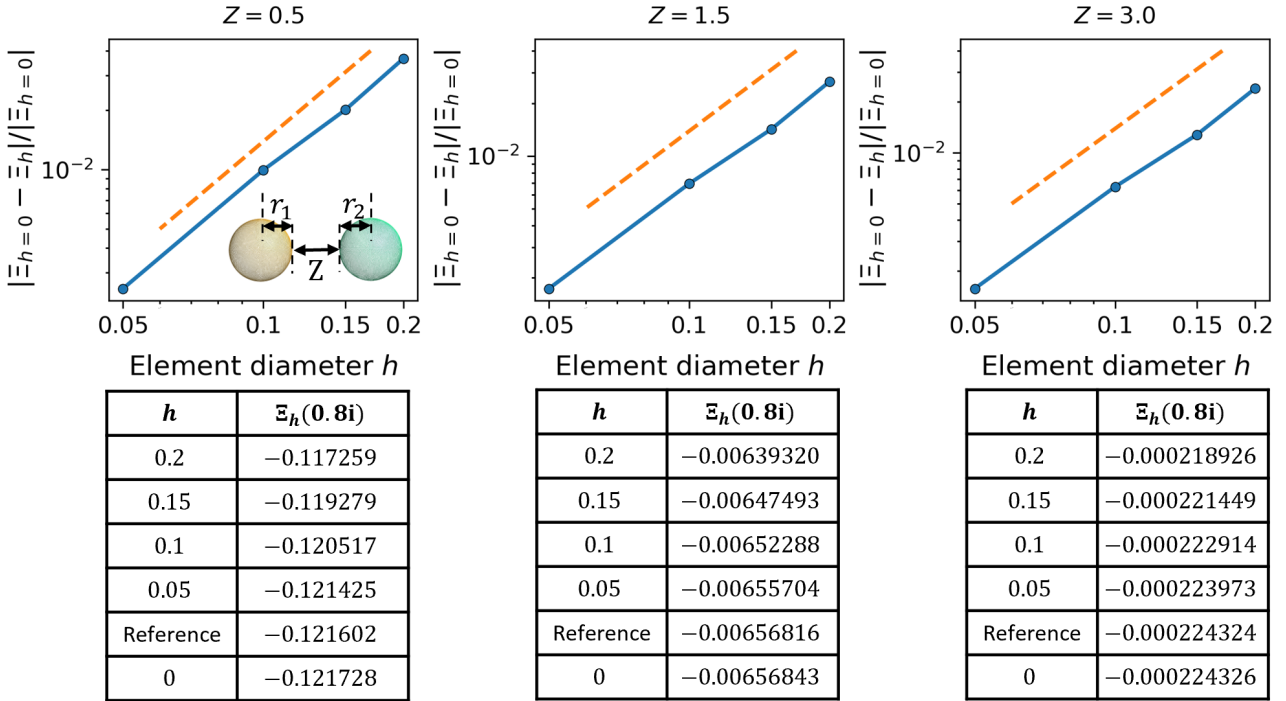


Figure 7: h -convergence of $\Xi_h(ik)$ to the extrapolation value $\Xi_{h=0}(ik)$ when $ik = 0.8i$. The provided reference values are accurate within 0.05%. The scatterers are two spheres with equal radii 1 and the distance between them is set as $Z = 0.5, 1.5$ and 3.0 . The relative distance between Ξ_h and $\Xi_{h=0}$ decreases as we refine the mesh. The dashed line shows order 2 convergence. The tables list the values of $\Xi_h(0.8i)$ for $h = 0, 0.05, 0.1, 0.15$ and 0.2 , and the provided reference values.

Having shown the validation of the construction of Ξ , we are left with determining a proper upperbound for the Casimir integration. The method for determining the upperbound of the integration is inspired by the asymptotic decay behavior of its integrand function. By Figure 1 and Figure 2, the integrand value $\log \det V(ik)\tilde{V}(ik)^{-1}$ shares the same trend with e^{-2Zk} , this inspires us to apply the function $f(k) = Ce^{-2Zk}$ to fit the curve of the estimated integrand values. With the coefficient C determined, one can estimate the absolute error for approximating the Casimir integral by computing:

$$\epsilon = \int_{\kappa}^{\infty} f(k) dk = \frac{Ce^{-2Z\kappa}}{2Z}, \quad (11)$$

where κ is the upperbound of the integration. Recall that we have changed the variable from k to $y = e^{-k}$ when applying the normal trapezoidal rule. This upperbound κ corresponds to the lowerbound of y .

With the upperbound of the integration determined, one can start to estimate the Casimir energy between two spheres with radius $r_1 = r_2 = 1$ at the distance of Z via the formula (5) in two different refinement levels: $h_{\text{fine}} = 0.05$ ($\dim(V_{ik}) = 12603$) and $h_{\text{coarse}} = 0.1$ ($\dim(V_{ik}) = 3192$).

Afterwards, the extrapolation result can be computed by these Casimir energy estimates. This result would

be regarded as the extrapolation value of the Casimir energy, which would be used to compare with the estimates derived from the asymptotic series introduced below.

According to [24], the Casimir energy between two spheres (with equal radii r) at asymptotically large separations can be obtained as a series in terms of the ratio of centre distance L ($l = 2r + Z$) to sphere radius R :

$$\zeta_{\text{asy}} = -\frac{\hbar c}{\pi} \frac{1}{L} \sum_{n=0}^{\infty} b_n \left(\frac{r}{l} \right)^{n+2}, \quad (12)$$

where the first six coefficients are $b_0 = -1/4$, $b_1 = -1/4$, $b_2 = -77/48$, $b_3 = -25/16$, $b_4 = -29837/2880$, $b_5 = -6491/1152$. Figure 8 shows the comparison between the Casimir energy computed from asymptotic series (12) and the exact value evaluated through Richardson extrapolation and the reference value ζ_{ref} provided in [26, Equation (64)]. Here, we observe that the asymptotic value gradually approaches to the exact value as the distance Z increases since the asymptotic expansion (12) only works when the distance between two spheres is asymptotically large.

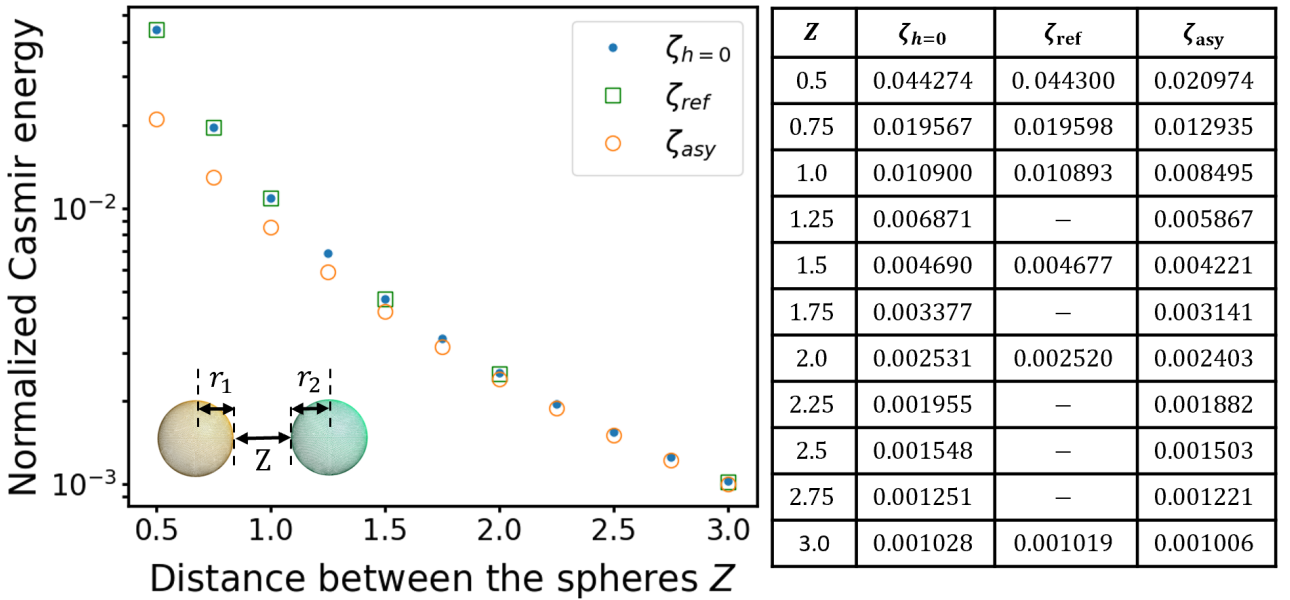


Figure 8: Left: Negative normalized Casimir energy ³computed by the extrapolation (blue circle), asymptotic series (orange hollow circle) in two spheres with equal radii's case. The radius is $r_1 = r_2 = 1$ and the distance Z ranges from 0.5 to 3.0. The green hollow square represents the data of [26]. Right: The table lists all the relevant data values in the figure.

³The negative normalized Casimir energy is $-\mathcal{E}/\hbar c$, for \mathcal{E} defined in (5).

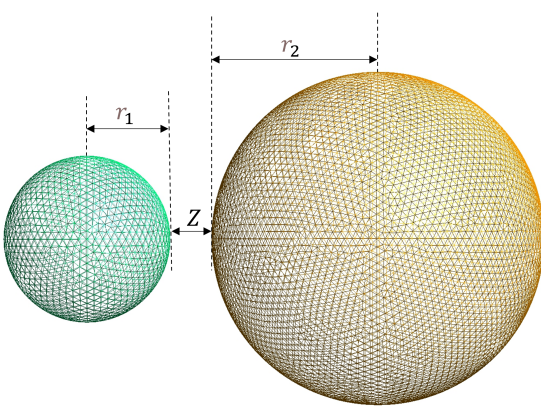


Figure 9: Two spheres with unequal radii $r_1 = 0.5$ and $r_2 = 1$ and Z is the minimal distance between them.

$h_{\text{coarse}} = 0.1$: $\dim(V_{ik}) = 2023$, N° of elements on both grids = 4038;

$h_{\text{fine}} = 0.05$: $\dim(V_{ik}) = 7891$, N° of elements on both grids = 15774

Now, let us consider the case when two spheres have different radii r_1, r_2 (see Figure 9).

In this case, one can still determine the upperbound of the integration by fitting the integrand function curve and considering the error tolerance. Afterwards, we would like to compare the extrapolation value of the Casimir energy computed through the Richardson extrapolation with the asymptotic expansion. By denoting the centre distance as $l = r_1 + r_2 + Z$, the asymptotic series of the Casimir energy between these two spheres is written by

$$\zeta_{\text{asy}} = -\frac{\hbar c}{\pi} \frac{1}{l} \sum_{n=0}^{\infty} \tilde{b}_n(\eta) \left(\frac{r_1}{L} \right)^{n+2}, \quad (13)$$

where the coefficients $\{\tilde{b}_n\}$ depend on the parameter $\eta = r_2/r_1$ and the first six coefficients are

$$\begin{aligned} \tilde{b}_0 &= -\frac{\eta}{4}, & \tilde{b}_1 &= -\frac{\eta + \eta^2}{8}, & \tilde{b}_2 &= -\frac{34(\eta + \eta^3) + 9\eta^2}{48}, & \tilde{b}_3 &= -\frac{2(\eta + \eta^4) + 23(\eta^2 + \eta^3)}{32}, \\ \tilde{b}_4 &= -\frac{8352(\eta + \eta^5) + 1995(\eta^2 + \eta^4) + 38980\eta^3}{5760}, & \tilde{b}_5 &= -\frac{-1344(\eta + \eta^6) + 5478(\eta^2 + \eta^5) + 2357(\eta^3 + \eta^4)}{2304}. \end{aligned}$$

In the following experiment, the radii of the spheres shown in Figure 9 are set as $r_1 = 0.5$ and $r_2 = 1$. As in the previous example, the exact value of the Casimir energy is computed through the Richardson extrapolation and the coarse and fine grid size are $h_{\text{fine}} = 0.05$ ($\dim(V_{ik}) = 7893$) and $h_{\text{coarse}} = 0.1$ ($\dim(V_{ik}) = 2023$), separately.

In this case, the asymptotic value of the Casimir energy was estimated by the series (13) and the comparison between the extrapolation value and asymptotic one is shown in Figure 10. Again, one can notice that when the distance between two spheres decreases, the asymptotic value gets close to the extrapolation one.

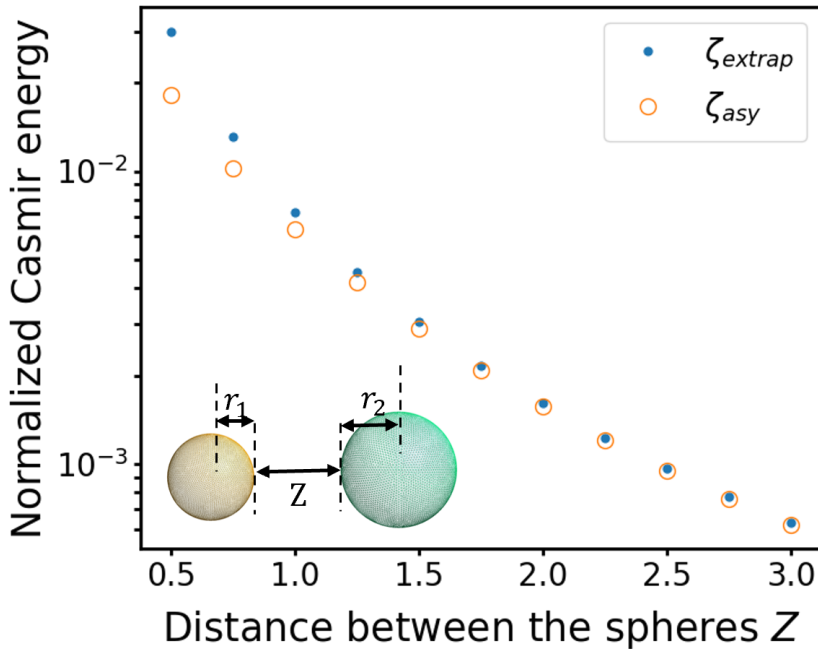


Figure 10: Negative normalized Casimir energy in two spheres with unequal radii's case. The radius is $R = 1$ and the distance Z ranges from 0.5 to 3.0. The exact value of the (negative normalized) Casimir energy has been written beside the data point, which is round up to 4 significant digits.

After showing the validation of the numerical framework for computing the Casimir energy, we would like to end this section with computing the negative normalized Casimir energy between one torus and one sphere. For the torus, it is centering at the origin and the distance from the center of the tube to the center of the torus is $l_1 = 2$ and the radius of the tube is $l_2 = 0.5$; for the sphere, it has radius $r = 1$ and its center is always on the z -axis (see Figure 11 (Right)). By Figure 11 (Left), one can see that when the sphere and the torus share the same center, the negative normalized Casimir energy has the largest magnitude. This means if one put this sphere at the origin in the beginning, this attractive effect will make the torus hold the sphere stationary.

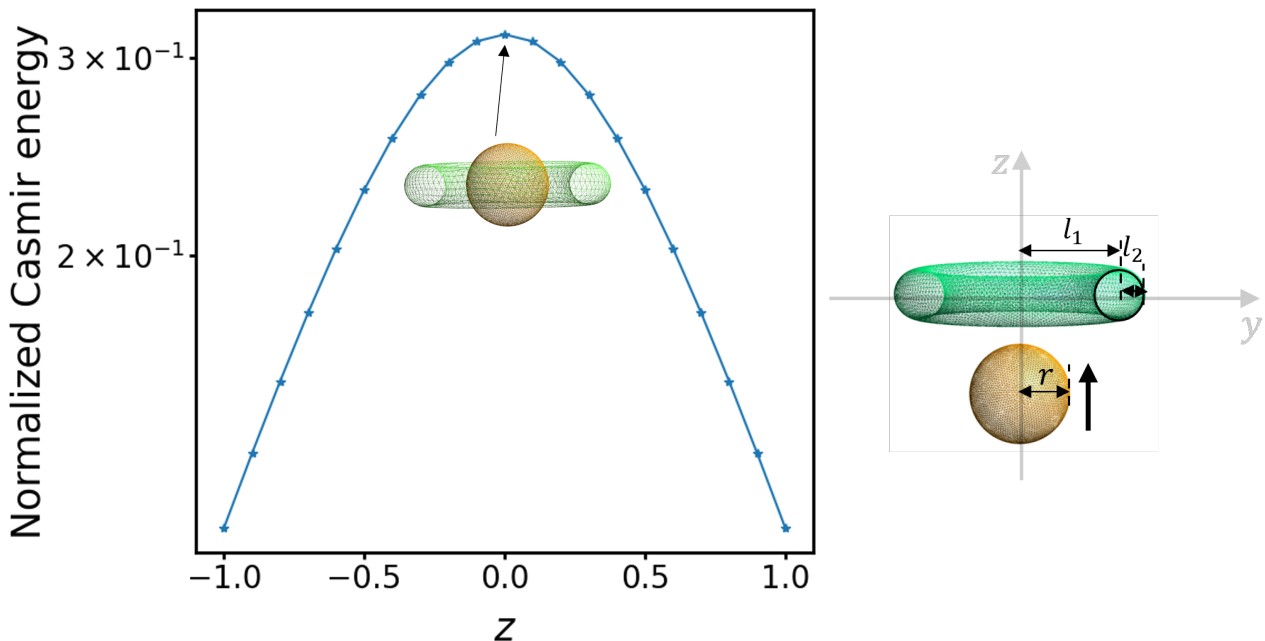


Figure 11: Negative normalized Casimir energy between a torus and a sphere when the sphere moves along the z -axis. The parameters of the torus are $l_1 = 2$, $l_2 = 0.5$ and the radius of the sphere is $r = 1$.

4.2. Realistic objects case

In this part, the Casimir energy between the objects with special shapes such as the menger sponges, ice crystals and ellipsoids will be computed through the Richardson extrapolation mentioned in the beginning of this section and the values labelled in the following figures are accurate within three significant digits. Note that the matrix size of the involved matrix in each example has been stated in the figures.

Figure 12 plots the menger sponges in different levels (0, 1 and 2) and the length of these sponges is always 1. Afterwards, the Casimir energy between two menger sponges in the same level are listed in Table 3. In addition, inside the extrapolation process, when $h_{\text{fine}} = 0.05$, the $\dim(V_{ik}) = 5664, 8510$ and 27136 and when $h_{\text{coarse}} = 0.1$, the $\dim(V_{ik}) = 1456, 3092$ and 14464 in different level (0, 1 and 2) cases, separately. By comparing the data point in this table, it is easy to find that the Casimir energy decreases as the number of the iteration increases since the cross-sectional area gets smaller.

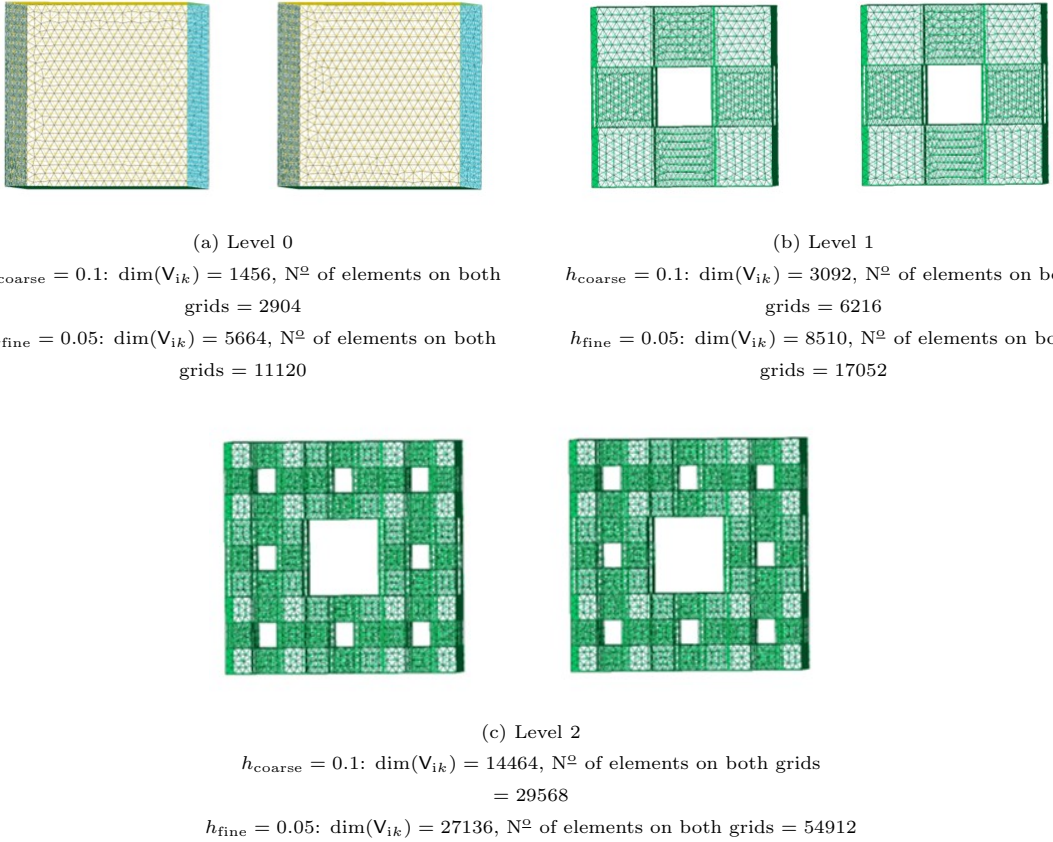


Figure 12: Menger sponges in different levels. The length of each sponge is 1.

Negative normalized Casimir energy in two menger sponges' case			
Distance	Level 0	Level 1	Level 2
0.5	0.08350	0.08229	0.08112
0.75	0.02737	0.02688	0.02670
1.0	0.01305	0.01288	0.01282
1.25	0.007357	0.007283	0.007252
1.5	0.004607	0.004568	0.004551
1.75	0.003099	0.003076	0.003065
2.0	0.002195	0.002181	0.002174
2.25	0.001618	0.001608	0.001603
2.5	0.001230	0.001223	0.001220
2.75	0.0009593	0.0009541	0.0009514
3.0	0.0007638	0.0007598	0.0007577

Table 3: Negative normalized Casimir energy in two menger sponges' case

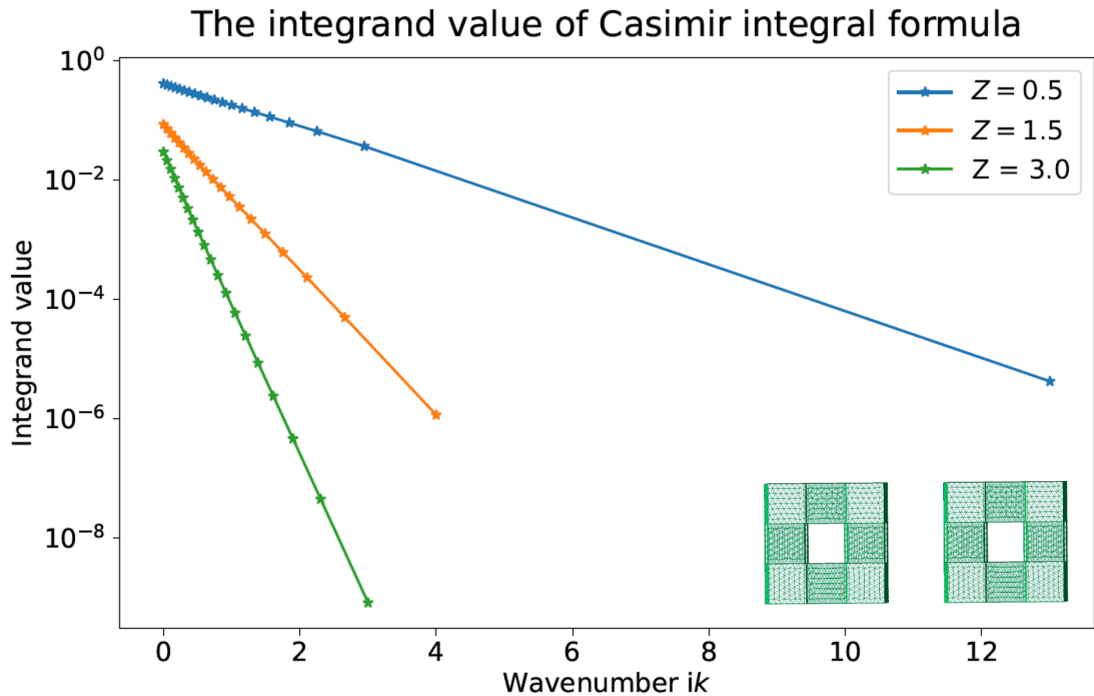


Figure 13: The integrand of the Casimir energy between two menger sponges in Level 1 with distance $Z = 0.5, 1.5$ and 3.0 .

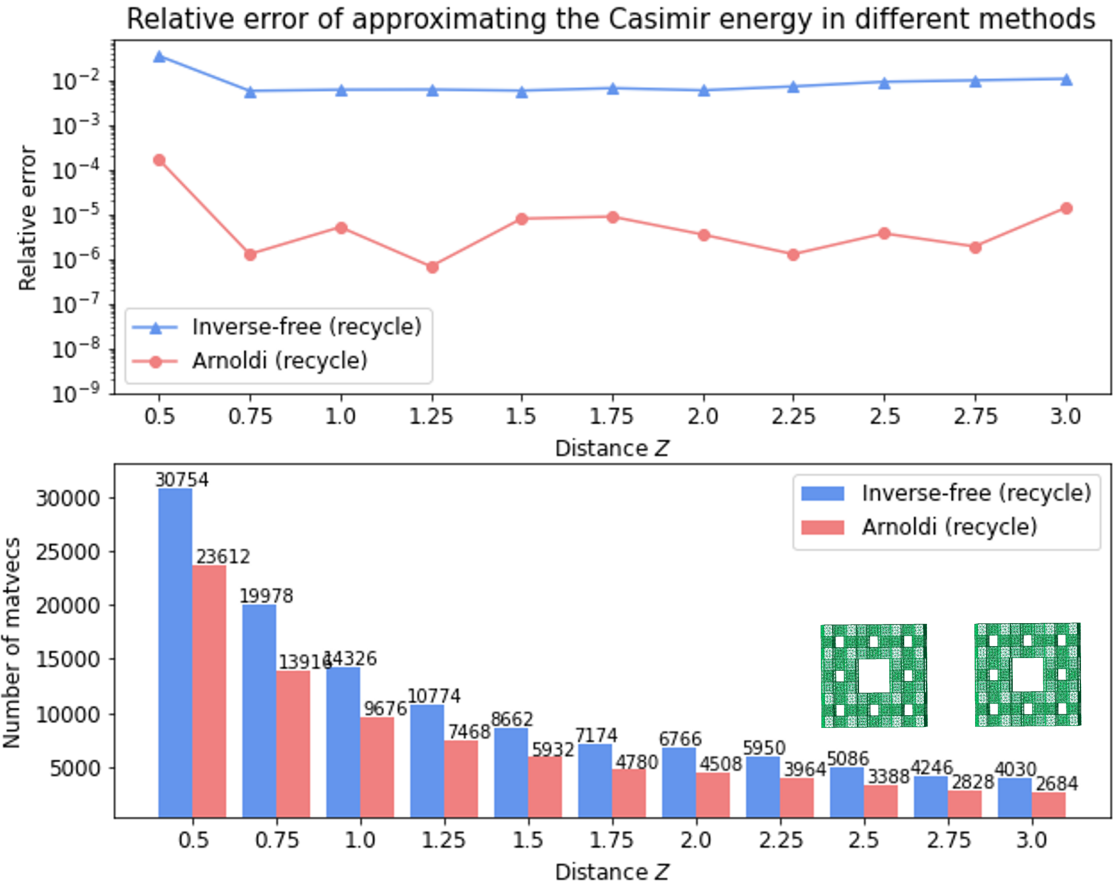
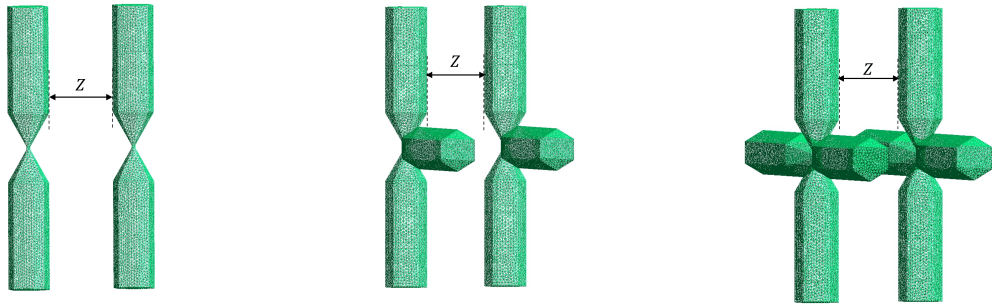


Figure 14: Menger sponges in Level 2's case: relative distance between the reference value (computed by Richardson extrapolation) with the estimates evaluated from the standard Arnoldi method with subspace recycled (solid red circles) and inverse-free Krylov subspace method with subspace recycled (solid blue triangles). The dimension of the Krylov subspace is $m = 100$. The recycled eigenvectors have the corresponding eigenvalue whose logarithm is larger than 10^{-5} .

In the next example, the scatterers are ice crystals with different number of branches ranging from 2 to 6 (see Figure 15).



(a) Two branches: $\dim(V_{ik}) = 8792$
 N^o of elements on both grids = 17576

(b) Three branches: $\dim(V_{ik}) = 13104$
 N^o of elements on both grids = 26200

(c) Four branches: $\dim(V_{ik}) = 17554$
 N^o of elements on both grids = 35100



(d) Five branches: $\dim(V_{ik}) = 21950$
 N^o of elements on both grids = 43900

(e) Six branches: $\dim(V_{ik}) = 26262$
 N^o of elements on both grids = 52556

Figure 15: Ice crystals with different number of branches

Negative normalized Casimir energy in ice crystals' case					
Distance	2-branches	3-branches	4-branches	5-branches	6-branches
0.5	0.04112	0.05989	0.07848	0.07873	0.01128
0.75	0.01499	0.02184	0.02855	0.02873	0.005017
1.0	0.007403	0.01080	0.01412	0.01428	0.002965
1.25	0.004242	0.006198	0.008113	0.008242	0.001985
1.5	0.002672	0.003905	0.005117	0.005223	0.001427
1.75	0.001797	0.002624	0.003442	0.003530	0.001074
2.0	0.001268	0.001849	0.002428	0.002501	0.0008357
2.25	0.0009288	0.001353	0.001776	0.001839	0.0006664
2.5	0.0007007	0.001019	0.001338	0.001391	0.0005410
2.75	0.0005413	0.0007863	0.001033	0.001078	0.0004469
3.0	0.0004270	0.0006188	0.0008134	0.0008526	0.0003741

Table 4: Negative normalized Casimir energy in 2- to 6-branched ice crystals' case

The integrand value of Casimir integral formula

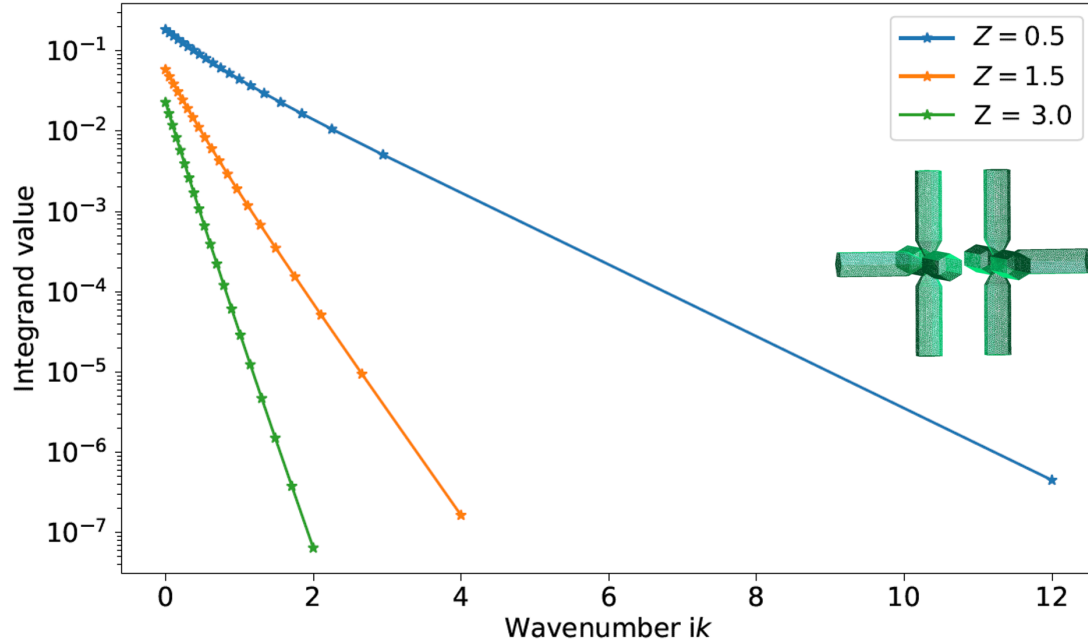


Figure 16: The integrand of the Casimir energy between two five-branches ice crystals with distance $Z = 0.5, 1.5$ and 3.0 .

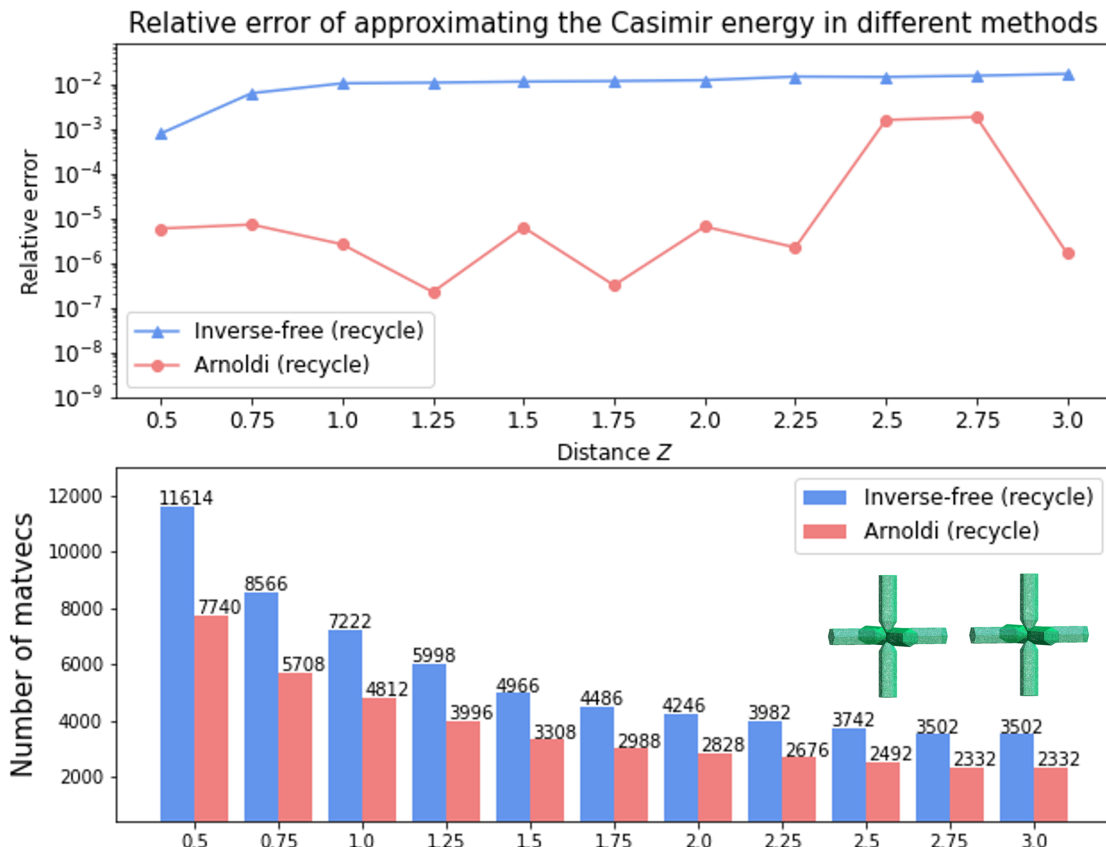


Figure 17: Six-branches ice crystals' case: relative distance between the reference value (computed by Richardson extrapolation) with the estimates evaluated from the standard Arnoldi method with subspace recycled (solid red circles) and inverse-free Krylov subspace method with subspace recycled (solid blue triangles). The dimension of the Krylov subspace is $m = 100$. The recycled eigenvector has the corresponding eigenvalue whose logarithm is larger than 10^{-5} .

It is not hard to imagine that the Casimir energy would be different when rotating the scatterers and keeping the distance between them unchanged. Therefore, in the last example, we would see how the Casimir energy between two identical ellipsoids changes as one of the ellipsoids rotates.

In Figure 18a, the above ellipsoid is centering at $(0, 0, 0)$ and the below one is centering at $(0, 0, -(0.5 + 0.5 + Z))$, where Z is the distance between these two ellipsoids. Without rotation, the Casimir energy between them with different distance Z is plotted in Figure 19a.

To explore how the rotation affects the change of the Casimir energy, one can always keep one ellipsoid fixed and rotate the other one. The Figure 18b and 18c describe the case when one of the ellipsoids rotates around z - and x -axis, respectively. From the Figure 19b, the Casimir energy changes periodically since we rotate one ellipsoid around z - or x -axis by 360 degrees.

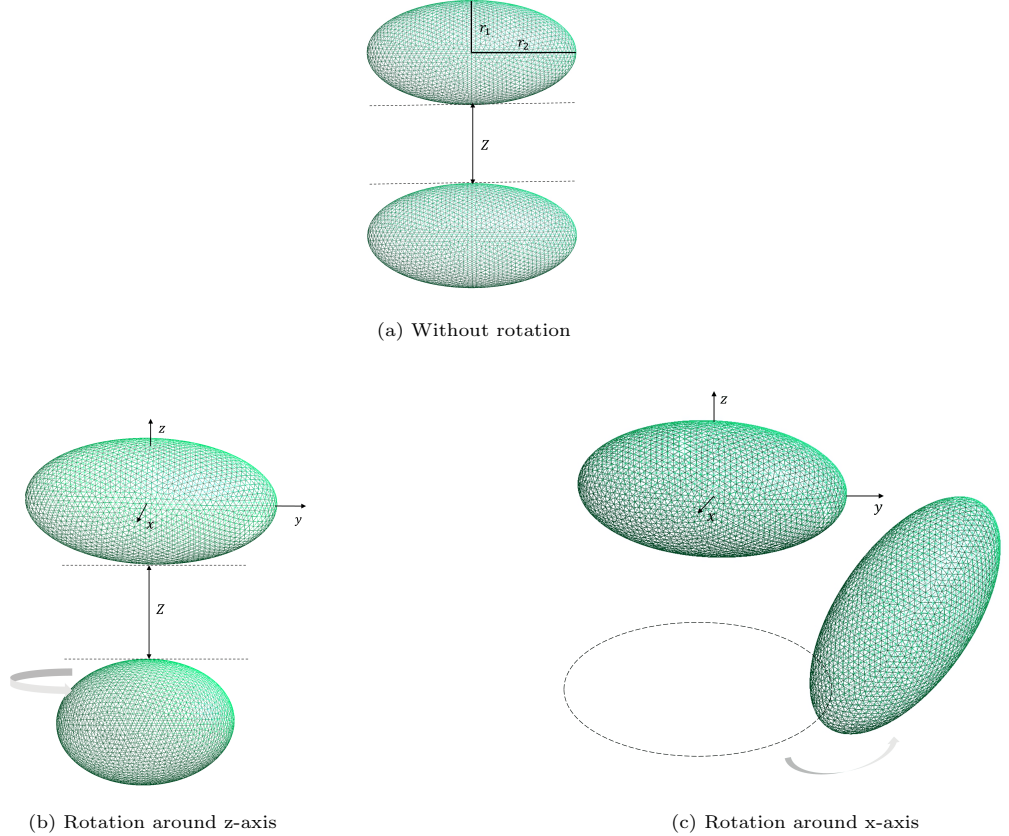
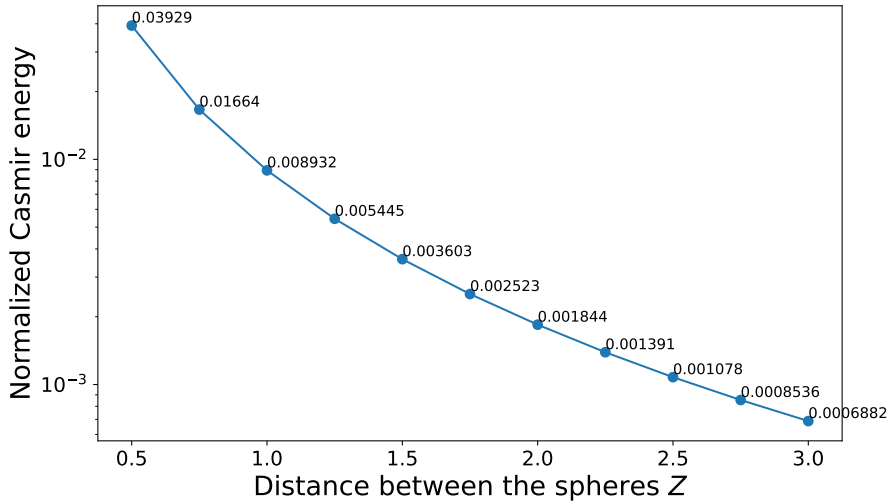


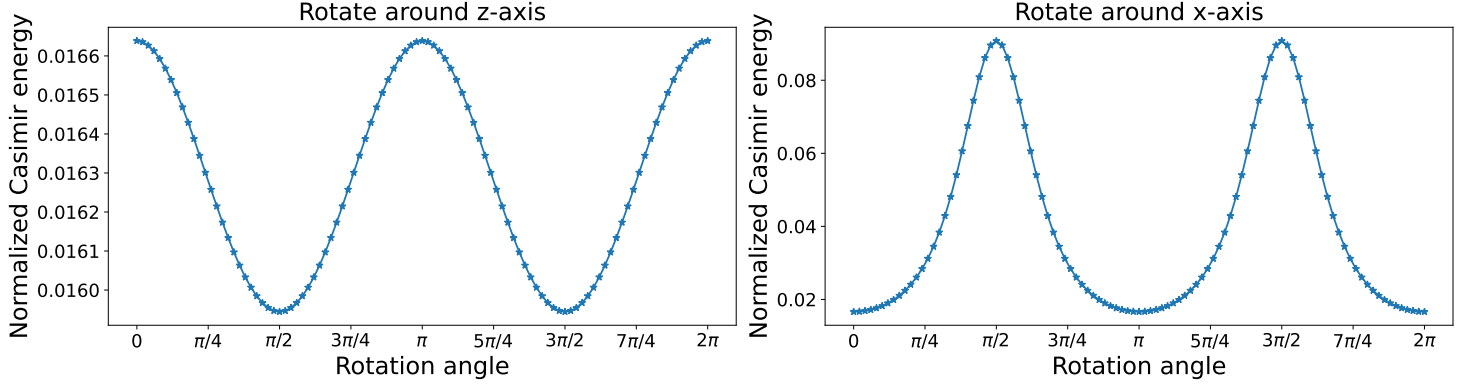
Figure 18: Two ellipsoids with or without rotation: when $h_{\text{fine}} = 0.05$, $\dim(V_{ik}) = 5517$; $h_{\text{coarse}} = 0.1$, $\dim(V_{ik}) = 1498$. The principal semi-axes of two ellipsoids are $r_1 = 0.5$ and $r_2 = 1.0$.

Casimir energy between two ellipsoids without rotations



(a) Casimir energy between two ellipsoids with different distances

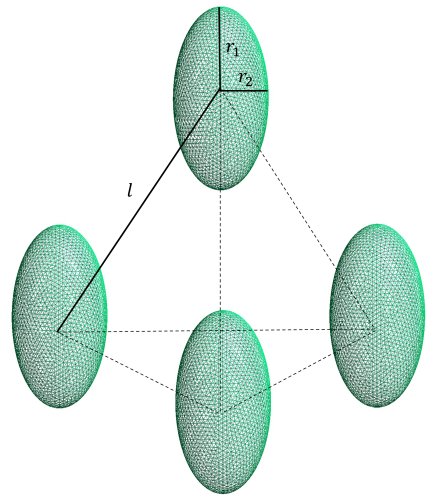
Casimir energy between two ellipsoids with rotations



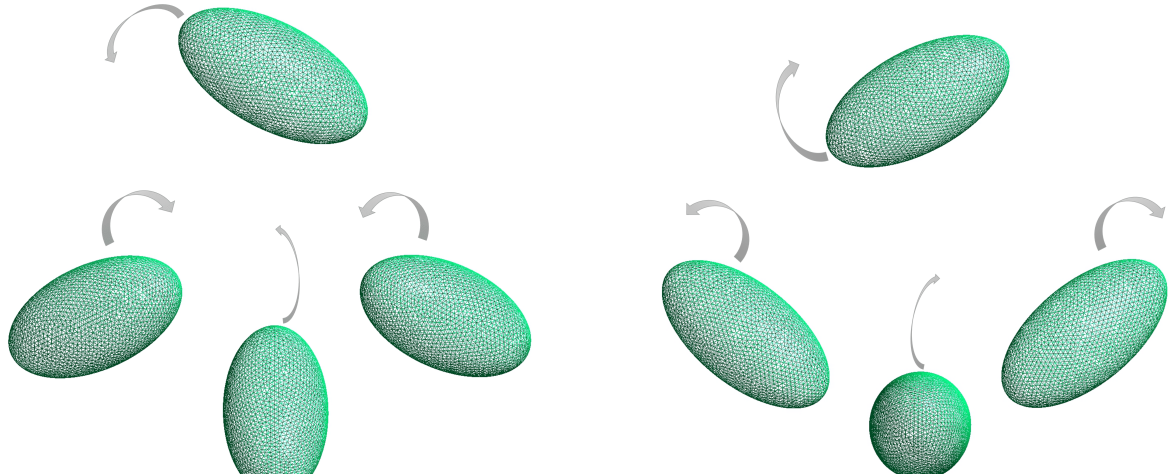
(b) Casimir energy when one of the ellipsoids rotates

Figure 19: The dependence of the Casimir energy and rotation angle of one of the ellipsoids.

Now, consider 4 ellipsoids located on the vertices of a regular tetrahedron with edge length $l = 2$ (Figure 20) and the principal semi-axes of all these ellipsoids are $r_1 = 0.6$ and $r_2 = 0.3$. Figure 20b and Figure 20c show the rotation of the ellipsoids inwards and outwards 360 degrees towards the centroid of this tetrahedron, separately. Afterwards, in order to use the Richardson extrapolation method to estimate the Casimir energy, we evaluate the integral (5) with the grid size set as $h_{\text{fine}} = 0.05$ and $h_{\text{coarse}} = 0.03$. Note that the number of the scatterers has increased to four, the matrices V_{ik} and \tilde{V}_{ik} have become to 4 by 4 block and diagonal block matrix, respectively. From the Figure 21, it shows that the Casimir energy between these four ellipsoids changes periodically with the rotation.



(a) No rotation



(b) Rotation inwards

(c) Rotation outwards

Figure 20: Four ellipsoids with or without rotations: when $h_{\text{fine}} = 0.03$, $\dim(V_{ik}) = 11024$; $h_{\text{coarse}} = 0.05$, $\dim(V_{ik}) = 4160$. The principal semi-axes of these ellipsoids are $r_1 = 0.6$ and $r_2 = 0.3$ and they locate on the vertices of a regular octahedron with edge length $l = 2$.

Casimir energy between four ellipsoids with rotations

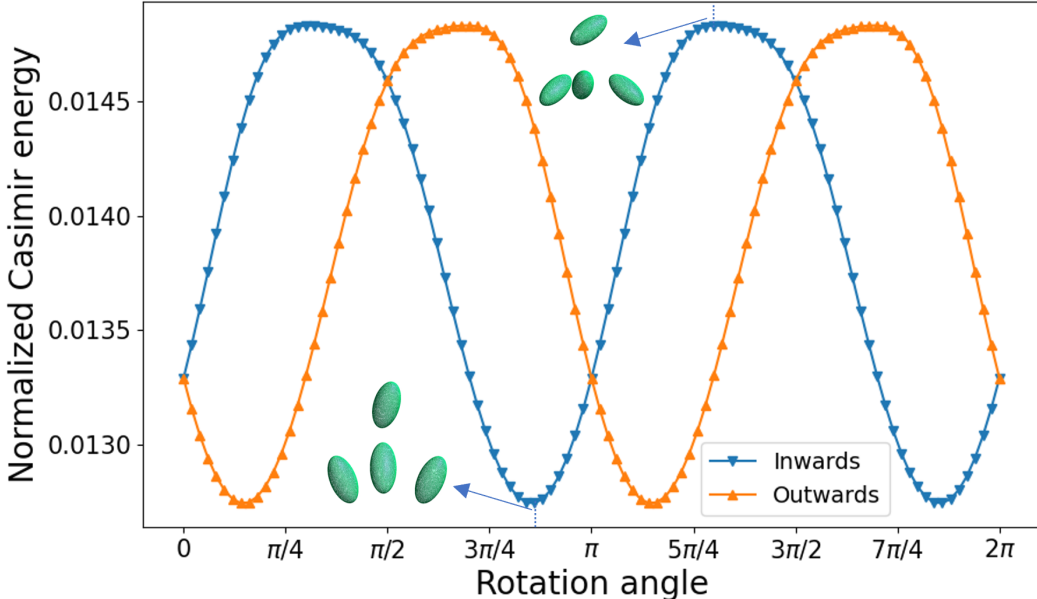


Figure 21: The dependence of the Casimir energy and rotation angle of one of the ellipsoids. Inwards towards the centroid case (solid blue square). Outwards towards the centroid case (solid orange triangle).

The scatterers of the last example are described inside the Figure 22. These six ellipsoids locate on the vertices of a regular octahedron with edge length $l = 2$ and again the principal semi-axes of all these ellipsoids are $r_1 = 0.6$ and $r_2 = 0.3$ (shown in the Figure 22). This time, the ellipsoids rotate inwards and outwards 360 degrees towards the centroid of this octahedron (Figure 22b and Figure 22c). By closely looking at these two rotation figures, we can notice that Figure 22b can be obtained by rotating Figure 22c 180 degrees. Therefore, the Casimir energies for the inwards and outwards cases are the same. Figure (23) shows how the Casimir energy changes among these six ellipsoids as they rotate.

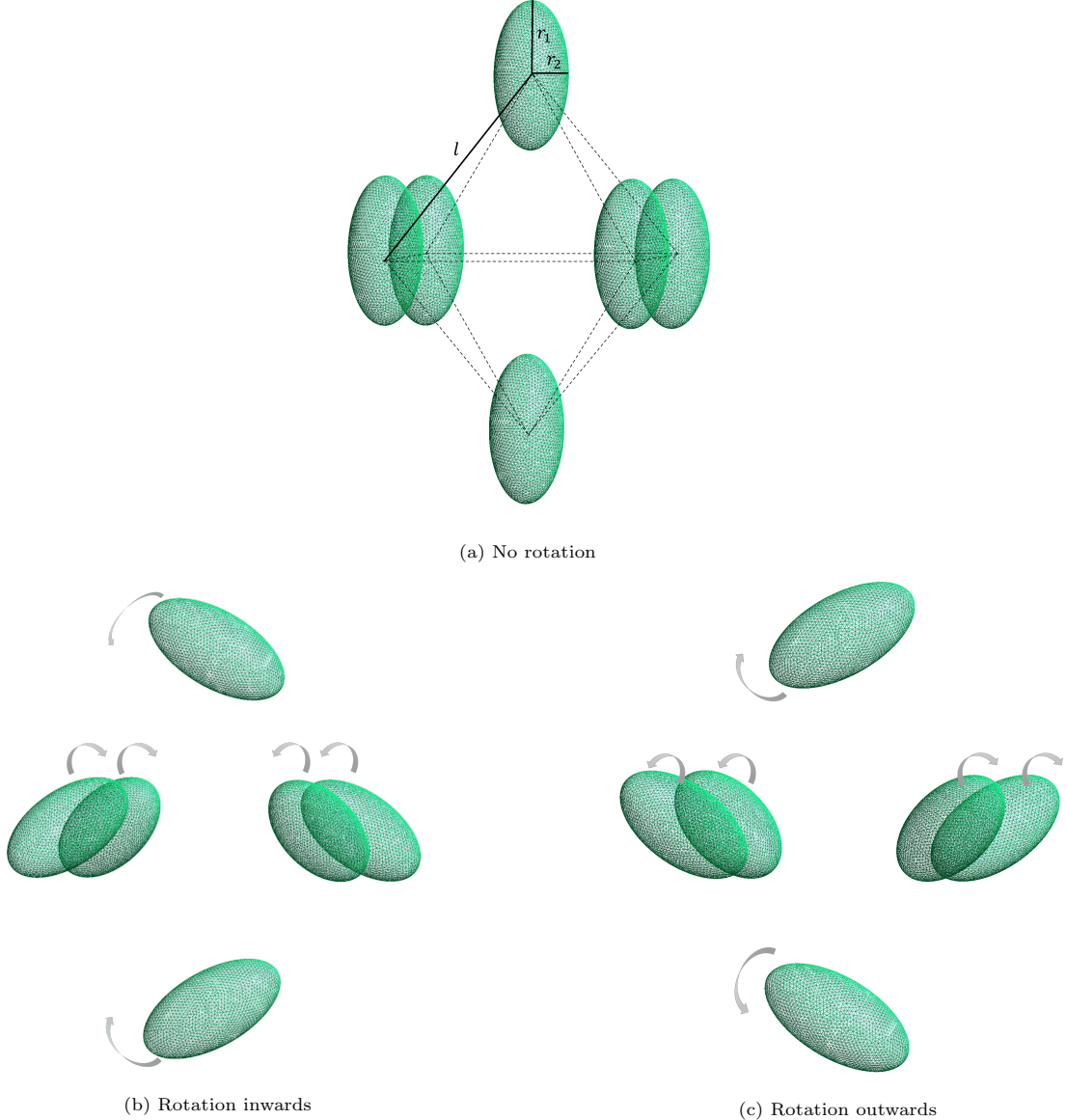


Figure 22: Six ellipsoids with or without rotations: when $h_{\text{fine}} = 0.03$, $\dim(V_{ik}) = 16536$; $h_{\text{coarse}} = 0.05$, $\dim(V_{ik}) = 6240$. The principal semi-axes of these ellipsoids are $r_1 = 0.6$ and $r_2 = 0.3$ and they locate on the vertices of a regular octahedron with edge length $l = 2$.

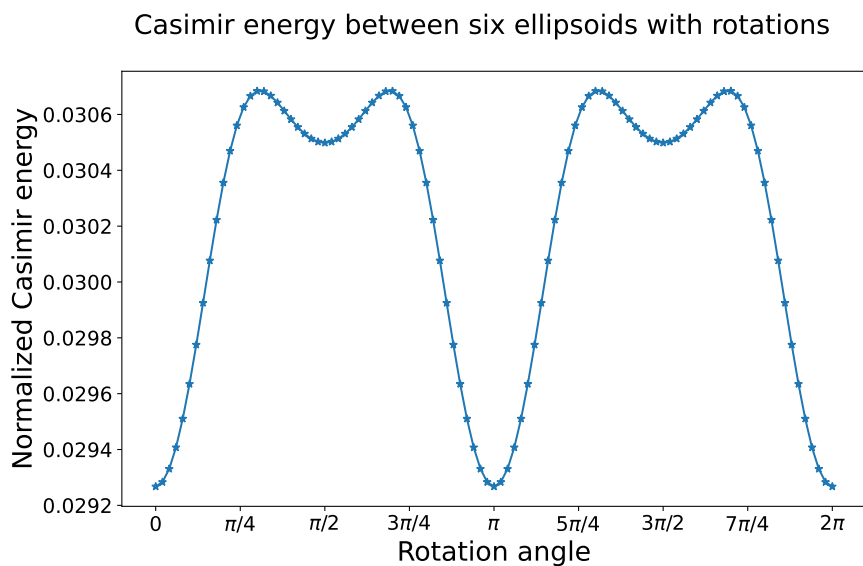


Figure 23: The dependence of the Casimir energy and rotation angle of one of the ellipsoids.

5. Conclusion

References

- [1] H. B. Casimir, On the attraction between two perfectly conducting plates, in: Proc. Kon. Ned. Akad. Wet., Vol. 51, 1948, p. 793.
- [2] M. J. Sparnaay, Measurements of attractive forces between flat plates, *Physica* 24 (6-10) (1958) 751–764.
- [3] S. K. Lamoreaux, Demonstration of the Casimir force in the 0.6 to 6 μ m range, *Physical Review Letters* 78 (1) (1997) 5.
- [4] T. Ederth, Template-stripped gold surfaces with 0.4-nm rms roughness suitable for force measurements: Application to the casimir force in the 20–100-nm range, *Physical Review A* 62 (6) (2000) 062104.
- [5] G. Bressi, G. Carugno, R. Onofrio, G. Ruoso, Measurement of the Casimir force between parallel metallic surfaces, *Physical review letters* 88 (4) (2002) 041804.
- [6] D. Krause, R. Decca, D. López, E. Fischbach, Experimental investigation of the Casimir force beyond the proximity-force approximation, *Physical review letters* 98 (5) (2007) 050403.
- [7] H. B. Chan, Y. Bao, J. Zou, R. Cirelli, F. Klemens, W. Mansfield, C. Pai, Measurement of the Casimir force between a gold sphere and a silicon surface with nanoscale trench arrays, *Physical review letters* 101 (3) (2008) 030401.
- [8] M. Bordag, U. Mohideen, V. M. Mostepanenko, New developments in the Casimir effect, *Physics reports* 353 (1-3) (2001) 1–205.
- [9] M. Bordag, G. L. Klimchitskaya, U. Mohideen, V. M. Mostepanenko, *Advances in the Casimir effect*, Vol. 145, OUP Oxford, 2009.
- [10] E. Elizalde, A. Romeo, Expressions for the zeta-function regularized Casimir energy, *Journal of mathematical physics* 30 (5) (1989) 1133–1139.
- [11] E. Elizalde, A. Romeo, Heat-kernel approach to the zeta-function regularization of the Casimir energy for domains with curved boundaries, *International Journal of Modern Physics A* 5 (09) (1990) 1653–1669.
- [12] K. Kirsten, *Spectral functions in mathematics and physics*, Chapman and Hall/CRC, 2001.
- [13] I. E. Dzyaloshinskii, E. M. Lifshitz, L. P. Pitaevskii, The general theory of van der waals forces, *Advances in Physics* 10 (38) (1961) 165–209.
- [14] L. S. Brown, G. J. Maclay, Vacuum stress between conducting plates: an image solution, *Physical Review* 184 (5) (1969) 1272.
- [15] D. Deutsch, P. Candelas, Boundary effects in quantum field theory, *Physical Review D* 20 (12) (1979) 3063.
- [16] B. S. Kay, Casimir effect in quantum field theory, *Physical Review D* 20 (12) (1979) 3052.
- [17] G. Scharf, W. Wreszinski, On the Casimir effect without cutoff, *Foundations of Physics Letters* 5 (5) (1992) 479–487.
- [18] S. A. Fulling, et al., Vacuum energy as spectral geometry, *SIGMA. Symmetry, Integrability and Geometry: Methods and Applications* 3 (2007) 094.

- [19] M. Renne, Microscopic theory of retarded van der waals forces between macroscopic dielectric bodies, *Physica* 56 (1) (1971) 125–137.
- [20] G. Bimonte, T. Emig, M. Kardar, M. Krüger, Nonequilibrium fluctuational quantum electrodynamics: Heat radiation, heat transfer, and force, *Annual Review of Condensed Matter Physics* 8 (2017) 119–143.
- [21] T. Emig, N. Graham, R. Jaffe, M. Kardar, Casimir forces between arbitrary compact objects, *Physical review letters* 99 (17) (2007) 170403.
- [22] T. Emig, R. Jaffe, M. Kardar, A. Scardicchio, Casimir interaction between a plate and a cylinder, *Physical review letters* 96 (8) (2006) 080403.
- [23] T. Emig, R. Jaffe, Casimir forces between arbitrary compact objects, *Journal of Physics A: Mathematical and Theoretical* 41 (16) (2008) 164001.
- [24] T. Emig, N. Graham, R. Jaffe, M. Kardar, Casimir forces between compact objects: The scalar case, *Physical Review D* 77 (2) (2008) 025005.
- [25] O. Kenneth, I. Klich, Opposites attract: A theorem about the Casimir force, *Physical review letters* 97 (16) (2006) 160401.
- [26] O. Kenneth, I. Klich, Casimir forces in a t-operator approach, *Physical Review B* 78 (1) (2008) 014103.
- [27] K. A. Milton, J. Wagner, Multiple scattering methods in Casimir calculations, *Journal of Physics A: Mathematical and Theoretical* 41 (15) (2008) 155402.
- [28] S. J. Rahi, T. Emig, N. Graham, R. L. Jaffe, M. Kardar, Scattering theory approach to electrodynamic Casimir forces, *Physical Review D* 80 (8) (2009) 085021.
- [29] F. Hanisch, A. Strohmaier, A. Waters, A relative trace formula for obstacle scattering, *Duke Math. J.* 171 (11) (2022) 2233–2274. doi:10.1215/00127094-2022-0053.
URL <https://doi.org/10.1215/00127094-2022-0053>
- [30] A. Strohmaier, The classical and quantum photon field for non-compact manifolds with boundary and in possibly inhomogeneous media, *Communications in Mathematical Physics* 387 (3) (2021) 1441–1489.
- [31] Y.-L. Fang, A. Strohmaier, A mathematical analysis of Casimir interactions i: The scalar field, in: *Annales Henri Poincaré*, Springer, 2021, pp. 1–51.
- [32] Y.-L. Fang, A. Strohmaier, Trace singularities in obstacle scattering and the Poisson relation for the relative trace, *Ann. Math. Qué.* 46 (1) (2022) 55–75. doi:10.1007/s40316-021-00188-0.
URL <https://doi.org/10.1007/s40316-021-00188-0>
- [33] M. W. Scroggs, T. Betcke, E. Burman, W. Śmigaj, E. van't Wout, Software frameworks for integral equations in electromagnetic scattering based on calderón identities, *Computers & Mathematics with Applications* 74 (11) (2017) 2897–2914.
- [34] A. Pietsch, *History of Banach spaces and linear operators*, Birkhäuser Boston, Inc., Boston, MA, 2007.
- [35] M. H. Reid, A. W. Rodriguez, J. White, S. G. Johnson, Efficient computation of casimir interactions between arbitrary 3d objects, *Physical review letters* 103 (4) (2009) 040401.

- [36] Y.-L. Fang, A. Strohmaier, Trace singularities in obstacle scattering and the poisson relation for the relative trace, *Annales mathématiques du Québec* 46 (1) (2022) 55–75.
- [37] R. Mathias, Quadratic residual bounds for the hermitian eigenvalue problem, *SIAM journal on matrix analysis and applications* 19 (2) (1998) 541–550.
- [38] W. E. Arnoldi, The principle of minimized iterations in the solution of the matrix eigenvalue problem, *Quarterly of applied mathematics* 9 (1) (1951) 17–29.
- [39] Y. Saad, Numerical methods for large eigenvalue problems, Vol. 66 of Classics in Applied Mathematics, Society for Industrial and Applied Mathematics (SIAM), Philadelphia, PA, 2011, revised edition of the 1992 original [1177405]. doi:10.1137/1.9781611970739.ch1.
URL <https://doi.org/10.1137/1.9781611970739.ch1>
- [40] G. H. Golub, Q. Ye, An inverse free preconditioned krylov subspace method for symmetric generalized eigenvalue problems, *SIAM Journal on Scientific Computing* 24 (1) (2002) 312–334.
- [41] J. H. Money, Q. Ye, Algorithm 845: Eigifp: A matlab program for solving large symmetric generalized eigenvalue problems, *ACM Transactions on Mathematical Software (TOMS)* 31 (2) (2005) 270–279.
- [42] Y. Saad, Numerical methods for large eigenvalue problems: revised edition, SIAM, 2011.